frontiers | Frontiers in Earth Science

TYPE Original Research
PUBLISHED 16 January 2023
DOI 10.3389/feart.2022.971738



OPEN ACCESS

EDITED BY
Zhuang Li,
China University of Petroleum, China

REVIEWED BY
Ye Qian,
Jilin University, China
Huichuan Liu,
China University of Petroleum, China

*CORRESPONDENCE
Yu Liu,
liuyuwh88@126.com

SPECIALTY SECTION
This article was submitted to Petrology, a section of the journal Frontiers in Earth Science

RECEIVED 17 June 2022
ACCEPTED 24 October 2022
PUBLISHED 16 January 2023

CITATION
Wu Y, Liu Y, Liu A, Tian L and Ye Y (2023), Geochronology and geochemistry of the Shanagen hydrothermal vein-type Mo deposit in Derbugan metallogenic belt of the NE China and their geological significance.
*Front. Earth Sci.* 10:971738.
doi: 10.3389/feart.2022.971738



# Geochronology and geochemistry of the Shanagen hydrothermal vein-type Mo deposit in Derbugan metallogenic belt of the NE China and their geological significance

Yunxia Wu[1,2,3], Yu Liu[2,3]*, Aoran Liu[2,3], Lifu Tian[2,3] and Yasheng Ye[3]

[1]College of Geoexploration Science and Technology, Jilin University, Changchun, China, [2]Hebei Key Laboratory of Strategic Critical Mineral Resources, Hebei GEO University, Shijiazhuang, China, [3]College of Earth Sciences, Hebei GEO University, Shijiazhuang, China

The Shanagen hydrothermal vein-type Mo deposit belongs to the Derbugan metallogenic belt, which is located in the Ergun block, NE China. The Mo mineralization is mainly developed in sericitized quartz siltstone around alkali-feldspar granite. In this paper, we present Molybdenite Re–Os dating, zircon U–Pb dating and geochemical data with the aim of determining metallogenic epoch and tectonic setting. Molybdenite Re–Os and zircon U–Pb dating of the alkali-feldspar granite indicate that the ore-formation and alkali-feldspar granite emplacement occurred at 143.1 ± 3.8 Ma, and 144.7 ± 0.7 Ma. Both were formed in the early Cretaceous. Chemically, the alkali-feldspar granites are enriched in L rare earth element and LILEs, depleted in H rare earth element and HFSEs, and pronounced negative Eu anomalies, are metaluminous and belong to the high-K calc-alkaline series and highly differentiated I-type granite. Geochemical features and concave upwards rare earth element pattern imply that alkali-feldspar granites were formed from magma generated by partial melting of lower crust. Combining the geochemistry, chronology, and the regional tectonic evolution, we infer that Shanagen hydrothermal vein-type Mo deposit was formed the extensional environment after the closure of the Mongol-Okhotsk Ocean.

KEYWORDS

**Derbugan metallogenic belt, Shanagen hydrothermal vein-type Mo deposit, zircon U, pb age, molybdenite Re-Os age, mongol-okhotsk ocean**

# 1 Introduction

The Derbugan metallogenic belt is one of the most important Cu–Mo–Pb–Zn–Ag–Au metallogenic belts in north China, bordering Mongol to the west and Russia to the north (Figure 1A; Zhu et al., 2001; Chen et al., 2006; Yang et al., 2009; Zhang L. C. et al., 2014). There have been discovered numerous porphyry Cu–Mo deposits (e.g., Wunugetushan, Taipingchuan, and Badaguan) and hydrothermal vein-type Pb–Zn–Ag deposits discovered (e.g., Jiawula et al., 2011; Zhao et al., 2017; Hui et al., 2021).

The now-extinct Mongol–Okhotsk Ocean exist in the Paleozoic and Mesozoic eras between the Siberian and Amur–North China continents block (Tomurtogoo et al., 2005; Domeier and Torsvik, 2014; Fritzell et al., 2016; Huang et al., 2016). The closure of the Mongol–Okhotsk Ocean created a suture zone that stretched 3,000 km eastward from the Khangai Mountains in northern Mongol to Uda Bay in East Okhotsk (Koval et al., 1999; Wang T. et al., 2015). It is largely accepted that the ocean closed in a scissor-like manner from southwest to northeast (Arzhannikova et al., 2022; Wang et al., 2022a). In addition to, the Mongol-Okhotsk Ocean closed from the late Paleozoic, gradually moved eastward, and finally closed from the Late Jurassic to the Early Cretaceous (Zorin, 1999; Kravchinsky et al., 2002; Cogné et al., 2005; Metelkin et al., 2007; Liu Y. et al., 2015; Van et al., 2015). Many studies have been made on the relationship between the mineralization of the Derbugan metallogenic belt and the evolution of the Mongol-Okhotsk Ocean in recent years (Zhang L. C. et al., 2014; Wang Y. H. et al., 2015; Gao et al., 2016; Niu et al., 2017; Mi et al., 2018). It is now widely accepted that the porphyry Cu-Mo deposit in Derbugan metallogenic belt was formed in the subduction of the Mongol-Okhotsk oceanic plate at the Triassic and Early-Middle Jurassic (Chen et al., 2010, Chen et al., 2011; Zhang et al., 2010; Zhang L. C. et al., 2014; Kang et al., 2014; Mi et al., 2021), and the hydrothermal vein-type Pb-Zn-Ag deposits in southwest of the Derbugan metallogenic belt were formed in an extensional environment after closure of the Mongol–Okhotsk Ocean (Nie et al., 2011; She et al., 2012; Cao and Liu. 2020). Furthermore, those Pb–Zn–Ag mineralization and Cu–Mo mineralization belong to a porphyry metallogenic system (Li et al., 2016; Hui et al., 2021). Moreover, some hydrothermal vein-type Pb-Zn-Ag deposits in central part of the Derbugan metallogenic belt were formed in a back-arc extension related to subduction of the Paleo-Pacific plate (Liang et al., 2020; Xu et al., 2020). The Shanagen Mo deposit is a newly discovered in Derbugan metallogenic belt, and it is different from the porphyry type Mo deposit and hydrothermal vein-type Pb-Zn-Ag deposit discovered in Derbugan metallogenic belt, and it is the only hydrothermal vein-type Mo deposit. Previous

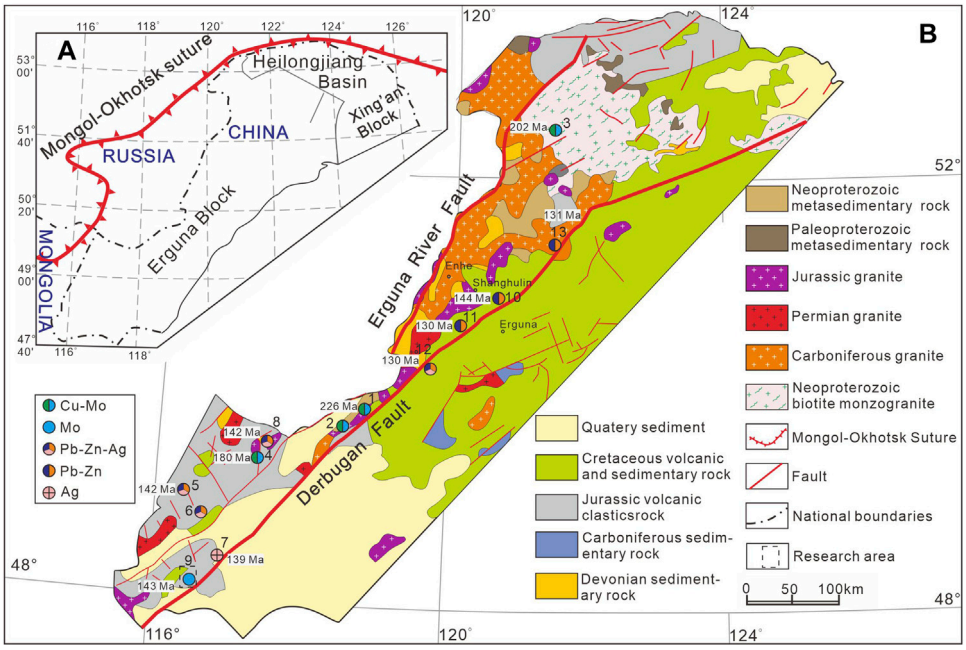


FIGURE 1
**(A)**Tectonic map of the Derbugan metallogenic belt; **(B)** Generalized regional geological map of the Derbugan metallogenic belt in Northeast China (after Chen et al., 2011). 1–Badaguan (Cu–Mo), 2–Babayi (Cu–Mo); 3–Taipingchuan (Mo), 4–Wunugetushan (Cu–Mo), 5–Jiawula (Pb–Zn–Ag), 6–Chaganbulagen (Pb–Zn–Ag), 7–Erentaolegai (Ag), 8–Halasheng (Pb–Zn), 9–Shanagen (Mo), 10 Derbugan (Pb-Zn), 11–Erdaohezi (Pb–Zn), 12–Dongjun (Pb–Zn), 13–Biliya (Pb–Zn).

10.3389/feart.2022.971738

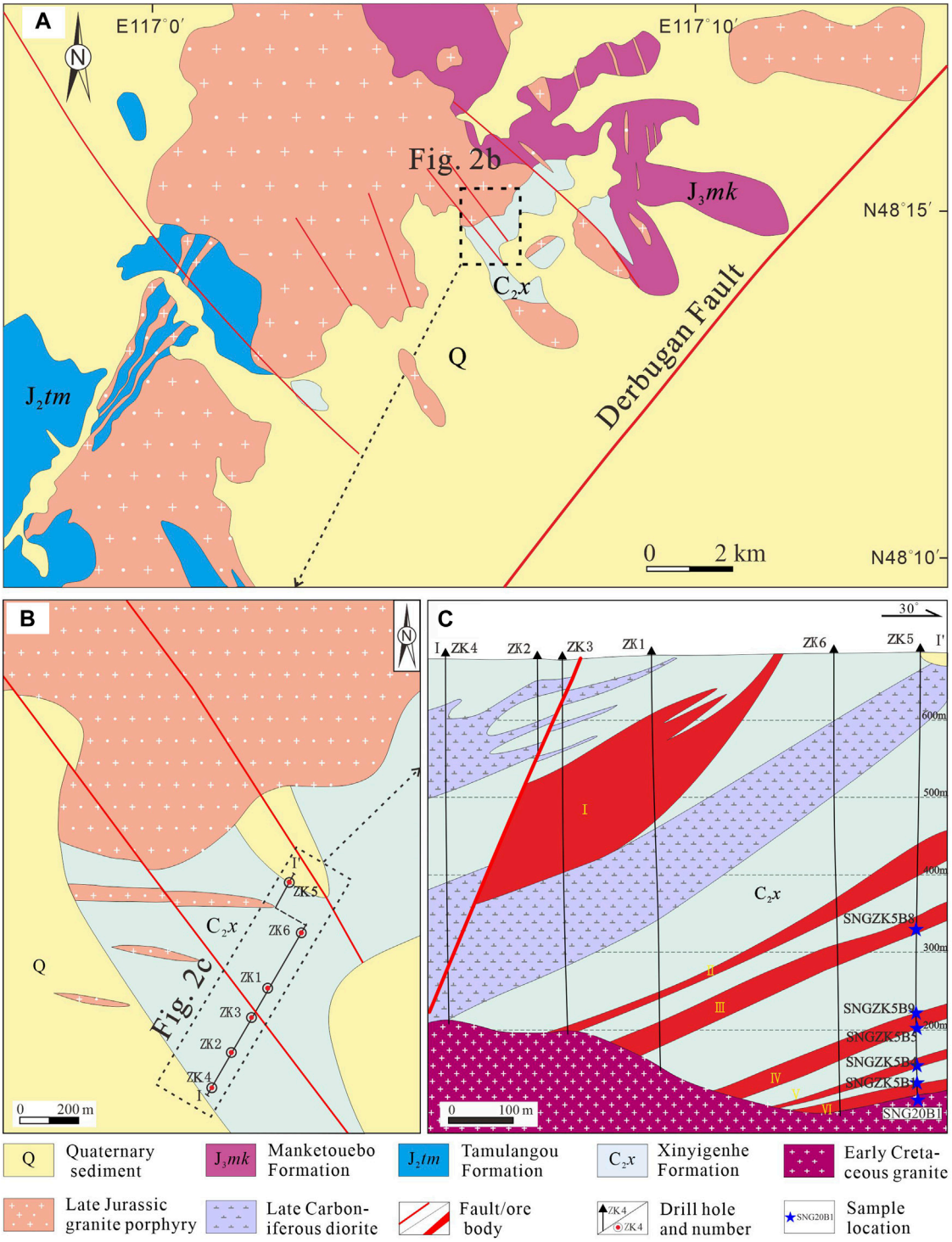


FIGURE 2
**(A)** Geological map of the Shanagen hydrothermal vein-type Mo deposit; **(B)** Drill hole distribution of Shanagen Mo deposit; c Cross-margin running NE-SW through the Shanagen Mo mine area.

studies mainly focused on the basic geological characteristics of the deposit and the spatial distribution of the ore body (Liu et al., 2014), There is still a lack of further research on the Shanagen deposit, such as metallogenic age, metallogenic background and intrusive rocks related to mineralization.

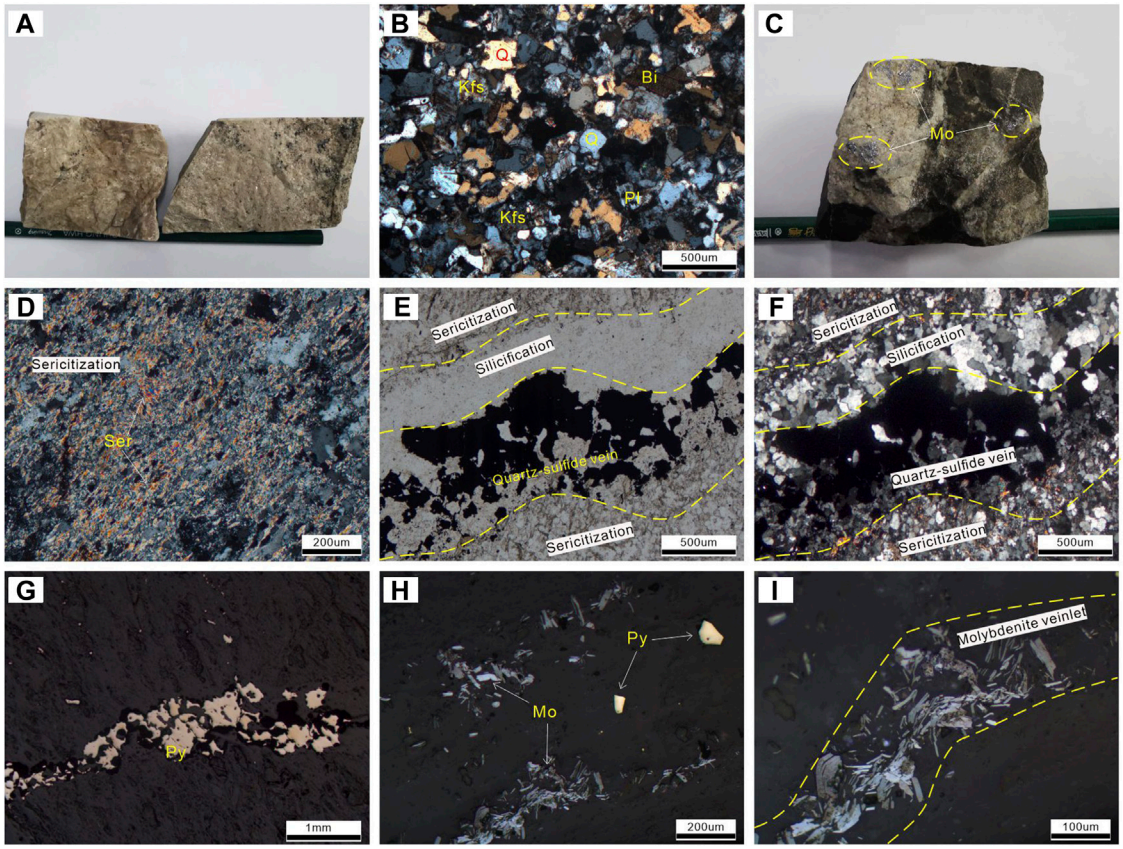


FIGURE 3
Photographs and photomicrographs of the alkali-feldspar granite and ore **(A)** Hand specimen of the alkali-feldspar granite, with granitic texture; **(B)** Quartz, plagioclase, potassium feldspar, and biotite in the alkali-feldspar granite; **(C)** Hand specimen of Mo ore with mass aggregate structure; **(D)** sericitization in Mo ore; **(E)**, **(F)** Quartz-sulfide veins in silicification and sericitization; **(G)** Pyrite veins; **(H)**, **(I)** Molybdenite veinlets. Q-quartz; Kf-K-feldspar; Pl-plagioclase; Bi-Biotite; Ser-Sericite; Py-Pyrite; Mo-Molybdenite.

Here we report molybdenite Re-Os geochronology of ore sample, zircon U-Pb ages and major and trace element compositions of alkali-feldspar granite. These data are used to determine the metallogenic age and constrain the tectonic setting of mineralization. It is hoped that our research can provide reference for the discovery of more hydrothermal vein-type Mo deposit in the Derbugan metallogenic belt.

## 2 Regional geology

The Erguna Block is located in the northwest of NE China, with Mongol-Okhotsk tectonic belt in the north and Xing'an Block in the south (Figure 1). The basement of the Erguna Block consists of Neoarchean amphibolite and metadiorite, Precambrian metamorphic supracrustal rocks, and Paleoproterozoic and Neoproterozoic granitoids (IMBGMR, 1991; Wu et al., 2012; Gou et al., 2013; Sun D. Y. et al., 2013; Tang et al., 2013; Liu et al., 2021). Neoarchean amphibolite and metadiorite were identified in the deep of the Villa area, and likely formed in an extensional continental arc/back-arc setting (Liu et al., 2021). Precambrian metamorphic supracrustal rocks are mainly exposed in Mohe area in the north west of the block and the east bank of Erguna River in the west, and can be were subdivided into Xinghuadukou Group, Luomahu Group and Jiageda Group (IMBGMR, 1991; Wu et al., 2012; Gou et al., 2013; Zhang S. H. et al., 2014; Mao, 2020), Paleoproterozoic granitoids were scattered in the Paleoproterozoic Xinghuadukou Group in the north of the Great Hinggan Mountains, and magma of the granitoids were mainly derived from an old Mesoarchean crustal source (Sun L. X. et al., 2013; Ge et al., 2015). Neoproterozoic granites are mainly biotite monzonitic granites, which are mainly distributed in the northeast part of Erguna massif, and may be generated by melting of a juvenile crust extracted from the mantle during (Guo et al., 2013). The exposed units are mainly Paleozoic shallow marine sandstones (IMBGMR, 1996) and widespread MesozoicLate terrestrial volcano–sedimentary sequence, including basalt and basaltic

andesite of Tamulangou Formation (172-161 Ma, Meng et al., 2011; Yang et al., 2022), rhyolite and rhyolitic tuff of Manketouebo Formation (162–148 Ma, Yin et al., 2019; Wang J. F. et al., 2019; Yang et al., 2022), andesite and trachyte of Manitu Formation (158-145 Ma, Sun et al., 2011; Shao et al., 2020; Yang et al., 2022), rhyolite of Baiyingolao Formation (141-123 Ma, Tan et al., 2017; Zhang et al., 2015; Li et al., 2018; Dong et al., 2020), and Meiletu Formation (133-120 Ma, Yang et al., 2019; Wu et al., 2019). The distribution characteristics of Mesozoic volcanic rocks indicate that the formations of Middle Jurassic -early Early Cretaceous volcanic rocks could be related to the evolution of the Mongol-Okhotsk suture zone, whereas the formation of the late Early Cretaceous volcanic rocks might be attributed to subduction of the Paleo-Pacific plate beneath the Eurasian continent (Meng et al., 2011; Xu et al., 2011; Wu et al., 2019; Yang et al., 2022).

Mesozoic intrusive rocks are developed in Erguna Block, which can be subdivided into Four stages according to the intrusion age, including Early-Middle Triassic, Late Triassic-Early Jurassic, Late Jurassic-early Early Cretaceous and late Early Cretaceous (Sun D. Y. et al., 2013; Xu et al., 2013; Tang et al., 2015; Tang et al., 2016a; Tang et al., 2016b; Mao, 2020). Early-Middle Triassic intrusive rocks are mainly monzogranite, syenogranite, quartz monzodiorite and granodiorite, are distributed in Badaguan and Erguna area, the north of Zixingtun Basin, the south of Jianjiatun Basin and the southwest of Shanghulin Basin (Mao, 2020). Magmatic association and arc-type geochemical characteristics of Early–Middle Triassic magmatism indicate that they were generated within an active continental margin setting related to the southward subduction of the Mongol–Okhotsk oceanic plate beneath the Erguna Massif (Deng et al., 2007; Sun D. Y. et al., 2013; Tang et al., 2015). Late Triassic-Early Jurassic intrusive rocks are mainly distributed in Mangui, Qiqian, Badaguan, Mohe and Mordaga areas, consist of gabbro, gabbro diorite, diorite, granodiorite, monzogranite, syenogranite and feldspar granite (Tang et al., 2016a; Mao, 2020). The magmatic association and geochemical characteristics of Late Triassic-Early Jurassic intrusive rocks are similar to those of the Early Middle Triassic, indicating the continuous southward subduction of the Mongolia Okhotsk oceanic crust beneath the Erguna massif (Sun D. Y. et al., 2013; Tang et al., 2014; Tang et al., 2016a; Liu et al., 2018). The intrusive rocks of Late Jurassic-early Early Cretaceous and late Early Cretaceous are mainly distributed in the Xiangyangtun basin and Shanghulin area. Those intrusive rocks consist of quartz monzonite, syenogranite, monzogranite, alkali feldspar granite, etc (Mao, 2020). Although the two magmatic activities were formed in an extensional environment, the intrusive rocks of Late Jurassic-early Early Cretaceous were related to collapse or delamination of a thickened part of the crust after closure of the Mongol–Okhotsk Ocean (Xu et al., 2013; Tang et al., 2015), While late Early Cretaceous intrusive rocks were attributed to the subduction of the Paleo-Pacific Plate beneath the Eurasian continent (Xu et al., 2013; Mao, 2020).

The dominant tectonic features in Erguna Massif are a SW–NE trending fault system in the younger crustal rocks and a NW–SE trending fault system in the basement (IMBGMR, 1991; Wu et al., 2012; Tang et al., 2015). The Mesozoic volcanism, plutonism and Metallogenesis were strongly controlled by the SW–NE trending fault system (Chen et al., 2011; Tang et al., 2015; Guo et al., 2016).

# 3 Geology of the deposit

The Shanagen hydrothermal vein-type Mo deposit is located at the southwest of the Derbugan metallogenic belt. The strata exposed in ore field include Quartz fine sandstone, quartz siltstone, and argillaceous siltstone of the Upper Carboniferous Xinyigenhe Formation ($C_2x$), and andesite of the Middle Jurassic Tamulangou Formation ($J_2tm$), and rhyolite, crystal tuff, tuffaceous sandstone of the Upper Jurassic Manketouebo Formation ($J_3mk$). The Xinyigenhe Formations host most of the Mo orebodies (Figures 2A,B), and the lithology is mainly quartz siltstone, argillaceous siltstone and a small amount of quartz fine sandstone. Intrusive rocks in the Shanagen ore field comprise Late carboniferous diorite and Late Jurassic granite porphyry and Early Cretaceous granite. The ore body is hosted in a series of NW-trending faults, and the dip angle of the ore body is 50°–60°. Six molybdenum ore bodies were found from top to bottom, of which No.I ore body is the main ore body (Figure 3C). The ore minerals are mainly pyrite, molybdenite, chalcopyrite and galena (Figures 3G,H). The hydrothermal alteration of ore is well developed, whose alteration types are mainly sericitization, silicification, pyritization and chloritization (Figures 3D–F).

# 4 Sampling and analytical methods

## 4.1 Samples preparation

Five samples of alkali-feldspar granite were collected from the granitic rocks around the ore body. Those samples are light flesh red and granite texture with massive structure, and contain quartz (~35%), alkali feldspar (~58%), plagioclase (~7%), and accessory minerals (Figures 3A,B). Five ore samples for Re-Os dating were collected from disseminated and agglomerated ores in the sericite alteration zone at a 520-to-680-m-deep of ZK5 (Figure 3C). Those samples undergo sericitization, silicification, and pyritization (Figures 3D–G). Molybdenite aggregates are distributed in veinlets (Figures 3H,I). A single molybdenite is scaly with a particle size of 0.05–0.5 mm.

TABLE 1 Zircon LA-ICP-MS results of the alkali-feldspar granite from Shanagen hydrothermal vein-type Mo deposit.

| Spot | Th | U | Th/U | Isotopic values | | | | | | Age (Ma) | | | | | |
|---|---|---|---|---|---|---|---|---|---|---|---|---|---|---|---|
| | | | | $^{207}Pb/^{206}Pb$ | 1σ | $^{207}Pb/^{235}U$ | 1σ | $^{206}Pb/^{238}U$ | 1σ | $^{207}Pb/^{206}Pb$ | 1σ | $^{207}Pb/^{235}U$ | 1σ | $^{206}Pb/^{238}U$ | 1σ |
| 1 | 1,214 | 2,757 | 0.44 | 0.0979 | 0.0094 | 0.1539 | 0.0583 | 0.0227 | 0.0008 | 1,584.9 | 179.8 | 140.1 | 4.0 | 144.9 | 5.1 |
| 2 | 676 | 581 | 1.16 | 0.0799 | 0.0075 | 0.1526 | 0.0396 | 0.0227 | 0.0007 | 1,194.4 | 185.2 | 144.7 | 11.6 | 144.6 | 4.5 |
| 3 | 233 | 155 | 1.50 | 0.1014 | 0.0081 | 0.1587 | 0.0370 | 0.0227 | 0.0006 | 1,650.0 | 148.1 | 146.2 | 9.1 | 144.5 | 3.6 |
| 4 | 1,264 | 1,022 | 1.24 | 0.1237 | 0.0115 | 0.1579 | 0.0457 | 0.0226 | 0.0006 | 2009.6 | 165.6 | 144.6 | 12.8 | 144.3 | 3.7 |
| 5 | 402 | 484 | 0.83 | 0.0800 | 0.0052 | 0.1588 | 0.0205 | 0.0227 | 0.0004 | 1,198.2 | 127.8 | 143.7 | 6.5 | 144.4 | 2.7 |
| 6 | 217 | 240 | 0.91 | 0.1112 | 0.0056 | 0.1487 | 0.0199 | 0.0225 | 0.0003 | 1820.4 | 92.4 | 143.7 | 15.0 | 143.6 | 2.0 |
| 7 | 158 | 364 | 0.43 | 0.1358 | 0.0057 | 0.1581 | 0.0192 | 0.0226 | 0.0003 | 2,173.8 | 77.9 | 141.8 | 13.7 | 144.4 | 1.9 |
| 8 | 323 | 298 | 1.08 | 0.1142 | 0.0067 | 0.1515 | 0.0291 | 0.0228 | 0.0005 | 1933.3 | 101.4 | 140.8 | 11.6 | 145.6 | 3.3 |
| 9 | 582 | 1785 | 0.33 | 0.1030 | 0.0049 | 0.1505 | 0.0235 | 0.0227 | 0.0005 | 1,679.6 | 88.6 | 147.6 | 10.8 | 144.5 | 3.0 |
| 10 | 1,213 | 880 | 1.38 | 0.1271 | 0.0053 | 0.1528 | 0.0235 | 0.0230 | 0.0004 | 2058.9 | 73.9 | 140.9 | 6.9 | 146.4 | 2.7 |
| 11 | 1,037 | 3,169 | 0.33 | 0.1194 | 0.0069 | 0.1552 | 0.0419 | 0.0227 | 0.0008 | 1947.8 | 102.6 | 149.7 | 9.8 | 144.6 | 5.1 |
| 12 | 725 | 645 | 1.12 | 0.0829 | 0.0038 | 0.1662 | 0.0160 | 0.0227 | 0.0005 | 1,277.8 | 88.9 | 139.6 | 12.8 | 144.9 | 3.3 |
| 13 | 959 | 1,030 | 0.93 | 0.0962 | 0.0028 | 0.1570 | 0.0118 | 0.0229 | 0.0004 | 1,553.7 | 54.2 | 141.8 | 9.2 | 145.9 | 2.3 |
| 14 | 336 | 305 | 1.10 | 0.0579 | 0.0019 | 0.1507 | 0.0066 | 0.0226 | 0.0003 | 524.1 | 74.1 | 148.7 | 5.7 | 144.2 | 2.2 |

## 4.2 Analytical methods

### 4.2.1 Zircon U–Pb dating

Zircons were extracted from whole-rock samples by using a combined magnetic and heavy liquid separation at Beijing GeoAnalysis Co. Ltd. Zircon grains were mounted in epoxy mounts at random, which were then polished to margin. All zircons were documented with transmitted and reflected light micrographs as well as cathodoluminescence (CL) images to reveal their internal structures. CL images of zircons were obtained at the Beijing GeoAnalysis Co. Ltd. with JEOL IT-500 SEM equipped with a Delmic CL system. Zircons U-Pb dating were performed using a quadrupole ICP-MS (iCAP RQ) and 193-nm ArF Excimer laser (RESOlution-LR) at Hebei GEO University. A zircon 91,500 standard was used for external age calibration, and zircon GJ-1 standard was used as a secondary standard to supervise the deviation of age calculation. For more detailed dating methods, see (Wang et al., 2022b; Wang et al., 2022c). ICPMSDataCal (Liu et al., 2010) and Isoplot (Ludwig, 2003) programs were used for data reduction. Isotope ratio and age uncertainties were quoted at the one sigma level. The zircon U–Pb isotopic data of the alkali-feldspar granite are presented in Table 1.

### 4.2.2 Whole rock major and trace element compositions

The whole-rock compositions of granite samples were completed in Beijing GeoAnalysis Technology Co.,Ltd. by X-ray fluorescence (XRF–1800; SHIMADZU) on fused glasses and inductively coupled plasma mass spectrometry (7,500; Agilent) after acid digestion of samples in Teflon bombs. Loss on ignition was measured after heating to 1,000°C for 3 h in a muffle furnace. The precision of the XRF analyses is within ±2% for the oxides greater than 0.5 wt% and within ±5% for the oxides greater than 0.1 wt%. Sample powders (about 40 mg) were dissolved in Teflon bombs using a HF + $HNO_3$ mixture for 48 h at about 190 °C. The solution was evaporated to incipient dryness, dissolved by concentrated $HNO_3$ and evaporated at 150°C to dispel the fluorides. The samples were diluted to about 80 g for analysis after re-dissolved in 30% $HNO_3$ overnight. An internal standard solution containing the element Rh was used to monitor signal drift during analysis. Analytical results for USGS standards indicated that the uncertainties for most elements were within 5%. The whole-rock geochemical data are presented in Table 2.

### 4.2.3 Re-Os dating of molybdenite

The Re-Os isotope composition of molybdenite was determined in the Key Laboratory of China, the Academy of Geological Sciences. Precisely weighed powders were loaded into Carius tubes together with $^{185}Re$ and $^{190}Os$ spikes and digested by reverse aqua regia, heated in an oven at 230 C for about 24 h. Osmium was separated using distillation and microdistillation, and Rhenium was extracted from the residue by acetone in an NaOH solution (Li et al., 2009,2010). Re and Os concentrations and isotopic compositions were measured by a Thermo Fisher Scientific Triton Plus mass spectrometer operating in negative ion detection mode (Li C. et al., 2015). The Re-Os isochron age

10.3389/feart.2022.971738

TABLE 2 Major and trace element data for alkali-feldspar granite from the Shanagen hydrothermal vein-type Mo deposit.

| Samples | SZK3-518 | SZK3-488 | SZK3-548 | SZK3-478 | SZK3-537 |
|---|---|---|---|---|---|
| $SiO_2$ | 76.6 | 77.0 | 76.8 | 76.5 | 76.7 |
| $TiO_2$ | 0.13 | 0.13 | 0.14 | 0.14 | 0.13 |
| $Al_2O_3$ | 12.6 | 12.3 | 12.4 | 12.6 | 12.5 |
| $Fe_2O_3$ | 0.75 | 0.53 | 0.81 | 0.77 | 0.79 |
| FeO | 0.42 | 0.27 | 0.41 | 0.30 | 0.40 |
| MnO | 0.01 | 0.02 | 0.03 | 0.02 | 0.04 |
| MgO | 0.21 | 0.28 | 0.26 | 0.27 | 0.18 |
| CaO | 0.54 | 0.69 | 0.57 | 0.65 | 0.55 |
| $Na_2O$ | 3.71 | 3.59 | 3.86 | 3.42 | 3.85 |
| $K_2O$ | 4.84 | 5.12 | 4.72 | 5.12 | 4.8 |
| $P_2O_5$ | 0.02 | 0.01 | 0.01 | 0.03 | 0.02 |
| Tatal | 99.8 | 99.9 | 100 | 99.8 | 100 |
| Mg# | 33.7 | 48.4 | 36.0 | 38.3 | 28.8 |
| $Na_2O+ K_2O$ | 8.55 | 8.71 | 8.58 | 8.54 | 8.65 |
| $Na_2O/K_2O$ | 0.77 | 0.70 | 0.82 | 0.67 | 0.80 |
| A/CNK | 1.02 | 0.97 | 0.99 | 1.02 | 1.00 |
| Li | 19.0 | 17.1 | 18.3 | 18.8 | 16.6 |
| Be | 8.87 | 8.01 | 8.77 | 7.51 | 8.16 |
| Sc | 3.70 | 3.04 | 3.80 | 2.97 | 3.56 |
| V | 14.0 | 15.4 | 11.0 | 15.7 | 15.4 |
| Cr | 3.02 | 2.43 | 1.27 | 2.92 | 3.10 |
| Co | 0.43 | 0.38 | 0.52 | 0.72 | 0.39 |
| Ni | 0.84 | 0.42 | 0.27 | 0.53 | 0.27 |
| Cu | 1.66 | 1.30 | 1.20 | 1.37 | 1.12 |
| Zn | 14.1 | 23.3 | 23.3 | 19.3 | 26.2 |
| Ga | 22.0 | 21.0 | 21.0 | 21.0 | 22.0 |
| Rb | 401 | 358 | 426 | 311 | 431 |
| Sr | 25.1 | 28.0 | 29.5 | 36.5 | 23.8 |
| Y | 9.87 | 14.0 | 12.2 | 11.9 | 13.0 |
| Zr | 106 | 80 | 97 | 100 | 113 |
| Nb | 42.4 | 50.6 | 42.9 | 37.7 | 38.2 |
| Ba | 60.9 | 69.7 | 68.8 | 91.7 | 54.9 |
| La | 48.5 | 51.3 | 45.4 | 43.2 | 44.1 |
| Ce | 67.4 | 73.0 | 66.7 | 66.0 | 62.7 |
| Pr | 4.92 | 5.98 | 5.65 | 5.73 | 5.11 |
| Nd | 14.2 | 16.0 | 15.6 | 16.1 | 13.6 |
| Sm | 1.68 | 2.09 | 2.05 | 2.31 | 1.81 |
| Eu | 0.19 | 0.18 | 0.22 | 0.29 | 0.20 |
| Gd | 1.47 | 1.99 | 1.79 | 1.88 | 1.66 |
| Tb | 0.26 | 0.26 | 0.29 | 0.28 | 0.25 |
| Dy | 1.17 | 1.42 | 1.57 | 1.33 | 1.49 |
| Ho | 0.27 | 0.37 | 0.33 | 0.29 | 0.37 |
| Er | 0.91 | 1.20 | 1.16 | 1.02 | 1.21 |
| Tm | 0.19 | 0.25 | 0.26 | 0.25 | 0.27 |
| Yb | 1.99 | 2.42 | 2.40 | 2.19 | 2.49 |
| Lu | 0.33 | 0.34 | 0.28 | 0.28 | 0.30 |
| Hf | 5.45 | 4.63 | 5.08 | 5.33 | 5.93 |
| Ta | 3.92 | 3.57 | 2.80 | 3.31 | 2.74 |

(Continued on following page)

TABLE 2 (*Continued*) Major and trace element data for alkali-feldspar granite from the Shanagen hydrothermal vein-type Mo deposit.

| Samples | SZK3-518 | SZK3-488 | SZK3-548 | SZK3-478 | SZK3-537 |
|---|---|---|---|---|---|
| Pb | 34.1 | 27.3 | 33.0 | 26.2 | 36.9 |
| Th | 48.2 | 43.3 | 51.1 | 44.4 | 49.5 |
| U | 14.0 | 18.0 | 14.0 | 23.0 | 13.0 |
| TotalTREE | 143 | 157 | 144 | 141 | 136 |
| LREE/HREE | 21 | 18 | 17 | 18 | 16 |
| $(La/Yb)_N$ | 16.4 | 14.3 | 12.8 | 13.3 | 11.9 |
| Ce/Ce* | 0.85 | 0.84 | 0.86 | 0.88 | 0.84 |
| Th/U | 3.44 | 2.41 | 3.65 | 1.93 | 3.81 |
| Eu/Eu* | 0.36 | 0.27 | 0.34 | 0.41 | 0.35 |

*Note*: Major element data are in percent; trace element data are in parts per million. REE, is rare Earth element; LOI, is loss on ignition. $Mg^{\#}$, $Mg^{2+}/(Mg^{2+}+TFe^{2+})$; A/CNK, mole $[Al_2O_3/(CaO + Na_2O + K_2O)]$; Eu/Eu*, {(Eu/0.0735)/[(Sm/0.1950) +(Gd/0.259)]/2}; $(La/Yb)_N$ = (La/0.310)/(Yb/0.209); Ce/Ce*, {(Ce/0.808)/[(La/0.310)+(Pr/0.122)]/2}.

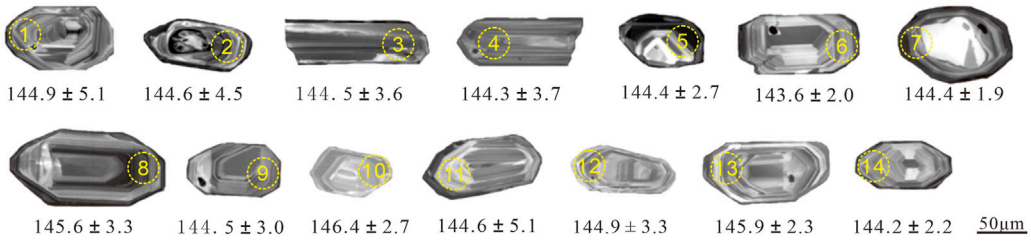


FIGURE 4
CL images of selected zircons from t alkali-feldspar granite samples in the Erguna Block. Yellow circles are the locations of U–Pb analyses.

was calculated by the Isoplot 3.0 program, and the decay constant used in the age calculation was $\lambda^{187}Re = 1.666 \times 10^{-11}year^{-1}$ (Smoliar et al., 1996). The uncertainty in Re-Os model ages includes 1.02% uncertainty in the$^{187}$Re decay constant and the uncertainty in Re and Os concentrations, which includes the weighing error for both spike and sample, as well as the uncertainty in spike calibration, and analytical error of the mass spectrometry.

# 5 Results

## 5.1 LA–ICP–MS zircon U–Pb age

The zircon LA–ICP–MS analysis data reveal that the U and Th contents and Th/U ratio are within the ranges of 155–3,169 ppm, 158–1,264 ppm, and 0.33–1.50, respectively (Table 1). Most of zircon grains selected for analysis are euhedral–subhedral and colorless, exhibit oscillatory growth zoning in their CL images (Figure 4). These properties indicate that zircons are magmatic origin (Hoskin and Schaltegger, 2003). The $^{206}Pb/^{238}U$ ages from 14 analytical spots range from 143.6 ± 2.0 to 145.9 ± 2.3 Ma, with a concordia age $^{206}Pb/^{238}U$ age of 144.7 ± 0.7 Ma (MSWD = 0.02) (Figure 5A).

## 5.2 Whole-rock geochemistry

The alkali-feldspar granites contain 76.5–77.0 wt% $SiO_2$, 12.3–12.6 wt% $Al_2O_3$, 0.53–0.81 wt% $Fe_2O_3$, 0.27–0.41 wt% FeO, 0.18–0.28 wt% MgO, 0.54–0.69 wt% CaO, 3.42–3.86 wt% $Na_2O$, and 4.80–5.12 wt% $K_2O$ (Table 2; Figure 6A; Streckeisen and Le Maitre, 1979; Le Maitre, 2002), are classified as high-K calc-alkaline series in $K_2O$ *versus* $SiO_2$ diagram, and are strongly metaluminous to weakly peraluminous (A/CNK, i.e., $Al_2O_3/(CaO+Na_2O+K_2O)$ = 0.97–1.02; Figures 6C,D, Peccerillo and Taylor, 1976; Maniar and Piccoli, 1989). They contain high total rare Earth element (REE) concentrations (136–157 ppm) and have right-declined and concave upwards REE pattern with evidently negative Eu anomalies (Eu/Eu* = 0.27–0.41), slightly negative Ce anomalies (Ce/Ce* = 0.84–0.88), and $(La/Yb)_N$ values of 11.9–16.4 (Figure 7A; Table 2; Sun and McDonough, 1989). These alkali-feldspar granites are also enriched in large ion lithophile elements (LILE, e.g., K, Rb), and are depleted in high field strength elements (HFSE, e.g., Ti. Figure 7B).

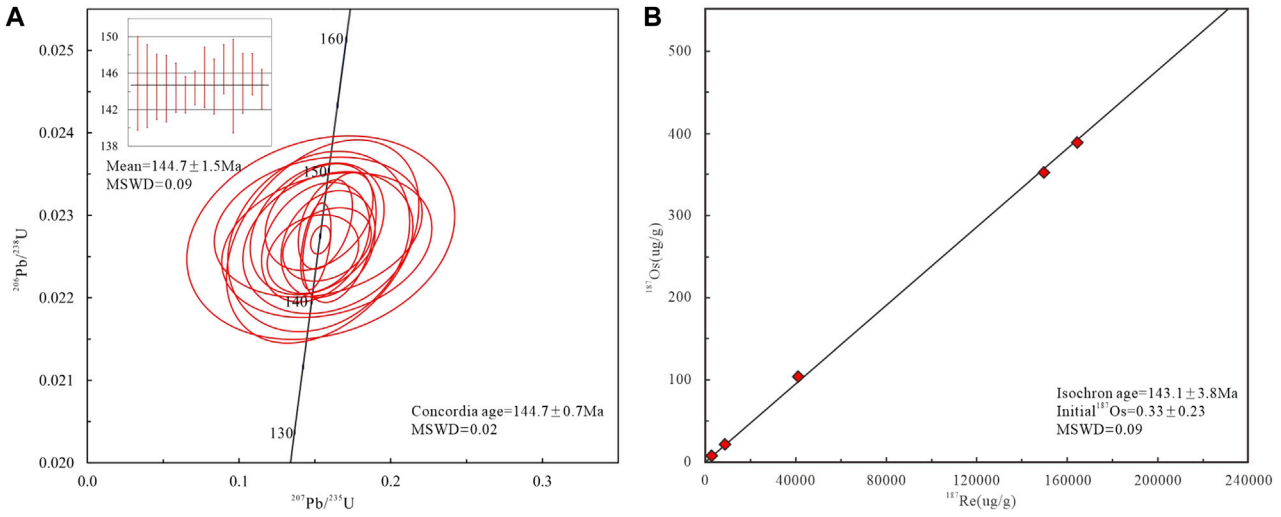


FIGURE 5
**(A)** U-Pb concordia diagrams for alkali-feldspar granite; **(B)** Re-Os isochron diagram for five molybdenite samples from the Shanagen hydrothermal vein-type Mo deposit.

## 5.3 Re-Os isotopic ages

The Re-Os isotopic data for the molybdenite samples are listed in Table 3, and are plotted in an isochron diagram in Figure 5B. The concentrations of Re and $^{187}Os$ range from 1,299 to 6,204 μg/g and from 816 to 3,899 ng/g, respectively. Five samples yielded model ages ranging from 141.49 ± 2.01 to 150.27 ± 2.27 Ma, and a well-constrained $^{187}Re$-$^{187}Os$ isochron age of 143.1 ± 3.8 Ma, with MSWD = 0.094 and an initial $^{187}Os$ of 0.33± 0.23 ng/g.

# 6 Discussion

## 6.1 Magmatism and mineralization of the derbugan metallogenic belt

The Delbugan metallogenic belt is located in the eastern part of the Central Asian orogenic belt, and its mineralization is closely related to the widespread Mesozoic magmatic activity (Ge et al., 2007; Zhang et al., 2010; Wu et al., 2014; Niu et al., 2016; Hui et al., 2021). The geochronological data of some metal deposits in the Derbugan metallogenic belt are listed in Table 4. According to the metallogenic epoch, age of intrusive rocks, and geochemical characteristics of intrusive rocks, the Debugan metallogenic belt can be divided into two series, one is Cu, Mo and Au deposits related to intermediate-acid intrusive rocks in the Late Triassic-Early Jurassic, the other is Pb-Zn-Ag polymetallic deposits related to intermediate-acid volcanic and intrusive activity in the Early Cretaceous (Zhang et al., 2010; Wu et al., 2014). The former are mainly porphyry Cu-Mo deposits and skarn Cu-Mo (Au) deposits (Wu et al., 2014; Zhang L. C. et al., 2014; Wang Y. H. et al., 2015; Gao et al., 2016), while the latter are mainly hydrothermal vein-type Pb-Zn-Ag polymetallic deposits (Niu et al., 2017; Wang J. X. et al., 2019; Xu et al., 2020; Hui et al., 2021). Porphyry Cu-Mo deposits are mainly distributed in the middle and north of the Derbugan metallogenic belt. Typical deposits include Taipingchuan Cu-Mo deposit and Badaguan Cu-Mo deposit. The wall rock alteration of these deposits is mainly sericitization and propylitization, and Cu-Mo mineralization is characterized by veinlets and disseminated (Chen et al., 2011; Wang et al., 2016; Mi et al., 2021). The porphyry related to mineralization belong to the high-K calc-alkaline series, and display a clear subduction-like signature including enrichment in LILEs and LREEs relative to HFSEs (Chen et al., 2010; Zhang et al., 2010; Li C. F. et al., 2014; Wang et al., 2017). Thus, the Magmatism and mineralization episode during Late Triassic-Early Jurassic are linked to the subduction of the Mongol–Okhotsk oceanic plate (Sun D. Y. et al., 2013; Zhang S. H. et al., 2014; Gao et al., 2016). Hydrothermal vein type deposits are mainly distributed in the middle and south of the Debugan metallogenic belt. Predecessors have conducted in-depth research on typical deposits such as Jiawula, Erentaolegai, Halaseng and Dongjun (Li C. F. et al., 2014; Xu et al., 2014; Yang et al., 2015; Wang J. F. et al., 2019; Hui et al., 2021). The distribution of ore bodies in these deposits is controlled by NW trending faults. Ore-body type is mainly sulfide-quartz vein, which occurs in andesite, basalt and trachyandesite of Tamlangou Formation. The hydrothermal-alteration assemblage is

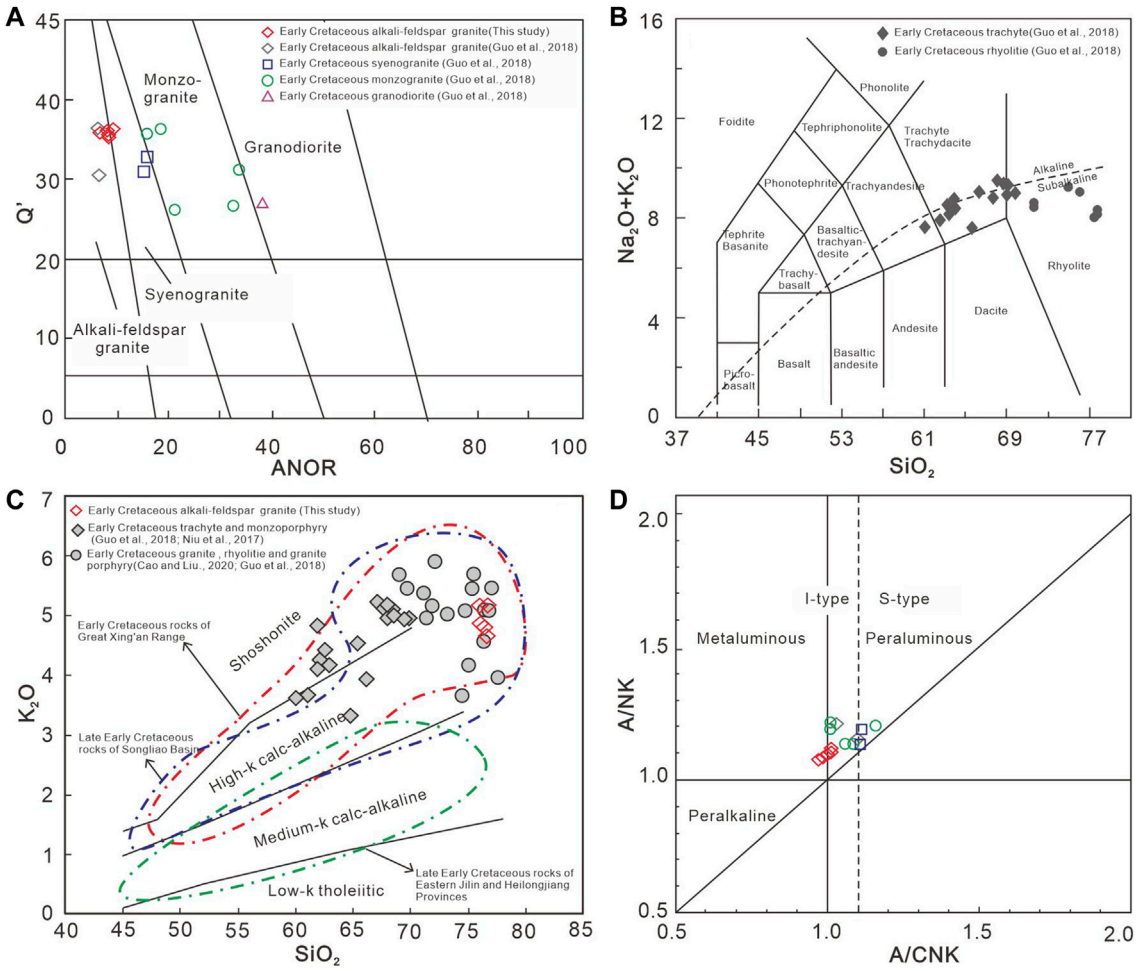


FIGURE 6
Classification and series diagrams of the alkali-feldspar granite. **(A)** Q′ *versus* ANOR diagram [Q′ = 100*Q/(Q + Ab + Or + An); ANOR = 100*An/(An + Or), Streckeisen and Le Maitre, 1979]; **(B)** Total alkalis *versus* $SiO_2$ diagram (Le Maitre, 2002); **(C)** $K_2O$ *versus* $SiO_2$ diagram (Peccerillo and Taylor, 1976), The data of dotted line area are from Guo et al. (2018); **(D)** A/NK *versus* A/CNK diagram (A/NK = $Al_2O_3/(Na_2O+ K_2O)$, A/CNK= $[Al_2O_3/(CaO + Na_2O+ K_2O$; Maniar and Piccoli, 1989).

generally silicification, sericitization, chloritization and carbonation (Li et al., 2016; Lü et al., 2020; Xu et al., 2020). It has been widely recognized that the Cretaceous Pb-Zn-Ag polymetallic deposits in the Debugan metallogenic belt were formed in an extensional setting (Li C. F. et al., 2014; Cao and Liu, 2020; Xu et al., 2020). Some researchers believe that Pb-Zn-Ag mineralization occur in back-arc extensional setting that was related to the subduction of the Paleo-Pacific Plate (Niu et al., 2017; Liang et al., 2020; Xu et al., 2020). However, other researchers attributed the mineralization to the orogenic extension after the closure of the Mongolia Okhotsk Ocean (Li C. F. et al., 2014; Zhao et al., 2017; Cao and Liu, 2020).

The Shanagan Mo deposit is the only hydrothermal vein-type Mo deposit in the Derbugan metallogenic belt. Previous studies have shown that granitoid intrusion are developed in hydrothermal vein-type Mo ore deposits, and mineralization is closely related to granitoid intrusion in space, time, and genesis (Zeng, et al., 2009; Fu et al., 2014; Yuan et al., 2020). The ore bodies of such deposits are distributed in granitoid and their surrounding rocks, and magma provides S element and main ore-forming hydrothermal fluid for Mo mineralization (Deng, et al., 2009; Yuan et al., 2020). The 144.7 ± 0.7 Ma zircon U-Pb age of the alkali-feldspar granite (Figure 5A) and 143.1 ± 3.8 Ma Re–Os isochron age of the molybdenite (Figure 5B) indicate that the Shanagen Mo deposit was formed in the early Cretaceous. According to the characteristics of hydrothermal vein-type Mo deposits and the metallogenic tectonic setting of the Derbugan metallogenic belt

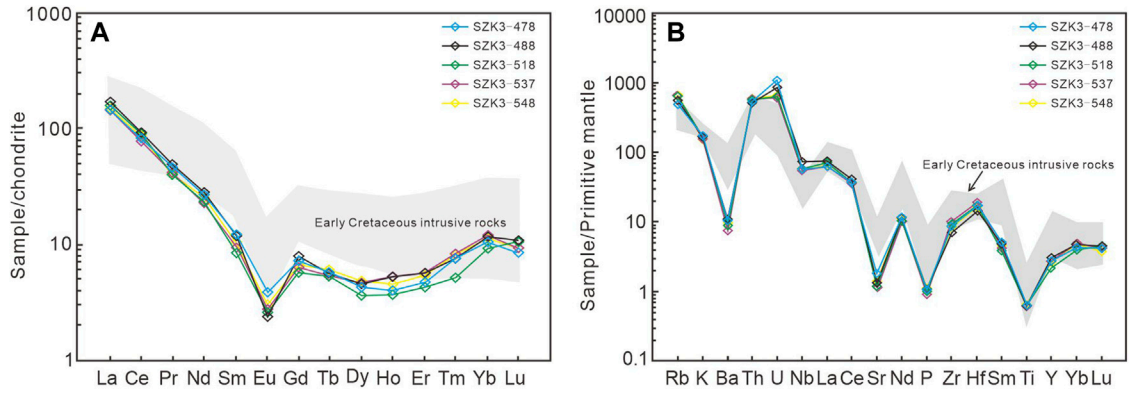


FIGURE 7
Chondrite-normalized rare Earth element and Primitive mantle-normalized trace element abundance spider diagram for the alkali-feldspar granite. Chondrite date from Boynton (1984); primitive-mantle date from Sun and McDonough (1989), the data of shadow area are from Niu et al. (2017), Guo et al. (2018), and Cao and Liu, (2020).

TABLE 3 Re–Os isotopic data for molybdenum from the Shanagen hydrothermal vein-type Mo deposit.

| Sample No. | Re/ng.g$^{-1}$ | | Os/ng.g$^{-1}$ | | $^{187}$Re/ng.g$^{-1}$ | | $^{187}$Os/ng.g$^{-1}$ | | Model age (Ma) | |
|---|---|---|---|---|---|---|---|---|---|---|
| | Measured | 2σ | Measured | 2σ | Measured | 2σ | Measured | 2σ | Measured | 2σ |
| SNGZK5B1 | 6,204 | 50 | 0.2005 | 0.0127 | 3,899 | 31 | 9.2 | 0.06 | 141.49 | 2.01 |
| SNGZK5B4 | 2,178 | 20 | 0.064 | 0.0089 | 1,369 | 12 | 3.23 | 0.02 | 141.62 | 2.12 |
| SNGZK5B5 | 1903 | 22 | 0.2231 | 0.035 | 1,196 | 14 | 3.01 | 0.02 | 150.69 | 2.63 |
| SNGZK5B8 | 1,329 | 9 | 0.7191 | 0.0085 | 835 | 6 | 2.03 | 0.01 | 145.43 | 1.96 |
| SNGZK5B9 | 1,299 | 12 | 2.2627 | 0.0189 | 816 | 7 | 2.05 | 0.01 | 150.27 | 2.27 |

in early Cretaceous, the mineralization of Shanagen hydrothermal vein-type Mo deposit was related to alkali feldspar granite, and formed in an extensional environment.

## 6.2 Petrogenesis of alkali-feldspar granites

The ca. 147.7 ± 0.7 Ma alkali-feldspar granites are metaluminous, and all of them have A/CNK<1.1 (Figure 6D). It is also shown that P2O5 is negatively correlated with SiO2, whereas Th is positively correlated with Rb (Figures 8A,B). Those features indicate that the alkali-feldspar granites are I-type granite (Harrison and Watson, 1984; Chappell and White, 1992; Chappell, 1999; Wu et al., 2007). Furthermore, the alkali-feldspar granites are characterized by strong enrichment of LREEs, pronounced negative Eu anomalies and relatively flat HREEs distributions, those REE patterns are like the REE curve of coeval I-type granite of the region (Figure 7A). All of sample show concave upwards REE pattern and relative depletion of middle REE with respect to HREE (Figure 7B). Such REE patterns are consistent with an origin involving partial melting of an amphibolitic source (Guo et al., 2018). In addition, the alkali-feldspar granites deplete of Eu, Ba, Sr, P and Ti (Table 2; Figures 7A,B), suggesting that these intrusions undergone the highly fractional crystallization (Irber, 1999; Patiño Douce and Castro, 1999; Wu et al., 2003). The fractional crystallization of plagioclase and potassium feldspar during magma cooling crystallization is responsible for the loss of Ba, Sr, and Eu, whereas fractional crystallization of apatite, ilmenite, and other accessory minerals cause the loss of P and Ti (Wu et al., 2003). The low $Al_2O_3/(FeO_T + MgO + TiO_2)$ ratios and $(Al_2O_3 + FeO_T + MgO + TiO_2)$ of alkali-feldspar granites also suggest the atalkali-feldspar granites are highly differentiated granite (Figure 8C, Patiño Douce and Castro, 1999). The high ratio of LREE/HREE (16–21) also strongly proves that the K-feldspar granite underwent differentiation.

Previous studies have shown that the highly differentiated I-type granites may have two genetic models: 1) fractional

TABLE 4 Geochronology data of some metal deposits in the Derbugan metallogenic.

| No. | Deposit | Wall rocks/ores | Analytical method | Age (Ma) | References |
|---|---|---|---|---|---|
| 1 | Badaguan porphyry Cu-Mo deposit | Quartz diorite porphyry/molybdenite | U-Pb/Re-Os | 229 ± 2/225± 2 | Gao et al. (2016) |
| | | Quartz diorite porphyry/molybdenite | U-Pb/Re-Os | 217 ± 2.6/222.4 ± 3.3 | Wang et al. (2016) |
| | | Molybdenite | Re-Os | 226.7 ± 2.4 | Li T. G. et al. (2014) |
| | | Granodiorite porphyry/molybdenite | U-Pb/Re-Os | 230.6 ± 2.8/228.7 ± 3.1 | Kang et al. (2014) |
| 2 | Babayi porphyry Cu-Mo deposit | | | | |
| 3 | Taipingchuan porphyry Cu–Mo deposit | molybdenite | Re-Os | 202.1 ± 9.4 | Wang et al. (2017) |
| | | Granodiorite porphyry/molybdenite | U-Pb/Re-Os | 202 ± 6/200 ± 5 | Zhang L. C. et al. (2014) |
| | | Sericite | Ar-Ar | 181.9 ± 1.1 | Mi et al. (2021) |
| 4 | Wunugetushan porphyry Cu-Mo deposit | Monzogranitic porphyry/Molydenite | U-Pb/Re-Os | 180.5 ± 2.0/180.4 ± 1.4 | Wang Y. H. et al. (2015) |
| | | Molydenite/Sericite | Re-Os/Ar-Ar | 177.6 ± 4.5/179.0 ± 1.9 | Chen et al. (2011) |
| | | Granite porphyry/molybdenite | U-Pb/Re-Os | 141.9 ± 2.4/135.4 ± 2.3 | Hui et al. (2021) |
| 5 | Jiawula hydrothermal vein-type Pb-Zn-Ag deposit | Quartz porphyry/Syenite porphyry/ monzonite porphyry | U-Pb | 150.1 ± 1.8/148.8 ± 2.2/ 145.3 ± 1.9 | Niu et al. (2017) |
| | | Pyrite and sphalerite | Rb-Sr | 142–143 | Li, (2016) |
| 6 | Chaganbulagen hydrothermal vein-type Ag-Pb-Zn deposit | Monzogranite porphyry/sericite | U-Pb/Ar-Ar | 143 ± 2/137 ± 3 | Li et al. (2016) |
| 7 | Erentaolegai hydrot- hermal vein-type Ag deposit | Quartz porphyry | U-Pb | 138.6 ± 2.3 | Xu et al. (2014) |
| | | Quartz porphyry/ore | U–Pb/Rb–Sr | 156/151 | Chen, (2010) |
| 8 | Halasheng hydrothermal vein-type Pb-Zn deposit | Alkali-feldspar granite | U-Pb | 142.4 ± 1.0 | Wang J. X. et al. (2019) |
| 9 | Shanagen hydrothermal vein-type Mo deposit | Biotite granite/molybdenite | U-Pb/Re-Os | 144.7 ± 0.7/143.1 ± 3.8 | This work |
| 10 | Derbur hydrothermal vein-type Pb-Zn deposit | Sphalerite | Rb–Sr | 141.6 ± 1.9 | Zhao et al. (2017) |
| 11 | Erdaohezi hydrothermal vein-type Pb-Zn deposit | Andesitic porphyry/Sulfide | U-Pb/Rb–Sr | 133.9 ± 0.9/130.5 ± 3.6 | Xu et al. (2020) |
| 12 | Dongjun hydrothermal vein-type Pb-Zn deposit | Sphalerite | Rb–Sr | 130.2 ± 4.4 | Yang et al. (2015) |
| 13 | Biliyagu hydrothermal vein-type Pb-Zn deposit | | | | |

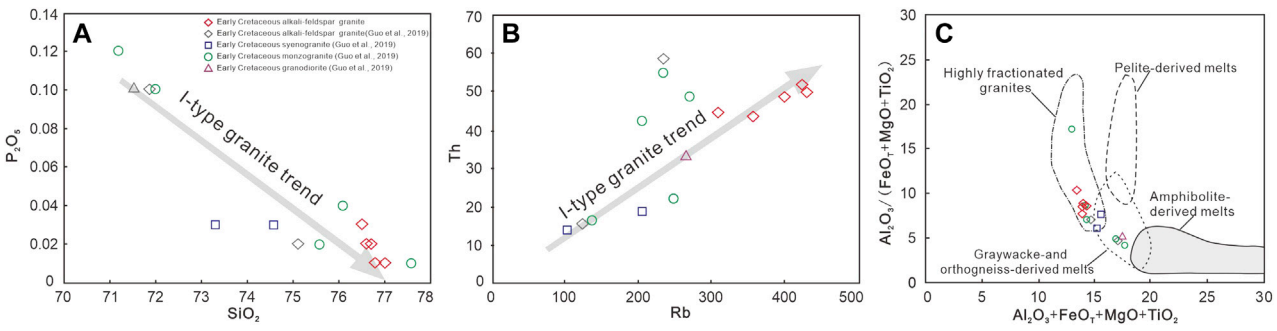


FIGURE 8
**(A)** $Al_2O_3/(FeO_T + MgO + TiO_2)$ *versus* $Al_2O_3 + FeO_T + MgO + TiO_2$ plot (Patiño Douce and Castro, 1999); **(B)** $CaO/Al_2O_3$ *versus* $CaO + Al_2O_3$ plot; **(C)** Rb/Ba *versus* Rb/Sr plot (Sylvester, 1998).

crystallization of a mafic, mantle magma, with or without crustal assimilation (Champion and Chappell, 1992; Fan et al., 2003); partial melting of crustal materials (Wu et al., 2003; Richards, 2011). If the alkali-feldspar granite magmas were generated by fractional crystallization of a mafic, mantle magma, then a fractionation sequence from basalt to rhyolite would have been observed. However, detailed geological mapping of the Mesozoic volcanic rocks in Shanagen ore district has shown that the basaltic rocks are mainly in the Tamulangou Formation, rhyolitic rock are mainly in Manketouebo Formation, and no other intervening mafic rocks exist (Figure 2). So, it seems unlikely they are derived from mafic magmas through fractional crystallization. The alkali-feldspar granites belong to the high-K calc-alkaline series, and displays a clear crustal magma signature, including pronounced negative Ba, Sr, and Ti anomalies, enrichment in Rb, Th, K, and LREEs (Figure 6C, Figures 7A,B, Harris et al., 1984; Bea et al., 2011; Dong et al., 2013). In addition, the upward concave REE model indicates that the magma came from amphibolite area. Therefore, the magma of alkali-feldspar granites likely originated from the partial melting of lower crust.

## 6.3 Metallogenic tectonic setting

The alkali-feldspar granites from Shanagen Mo deposit and Early Cretaceous granitic intrusive rocks in Erguna Block are enriched in LILEs (e.g., K, Rb) and LREE elements, and depleted in HFSEs (e.g., Ti) and HREE elements (Figures 7A,B; Niu et al., 2017; Guo et al., 2019; Cao and Liu, 2020), showing geochemical features similar to subduction-related and/or post-collisional magmas (Roberts and Clemens 1993). Thus, two geodynamic models (subduction of the Palaeo-Pacific Plate and post-orogenic extension after closure of the Mongol-Okhotsk Ocean) should be considered.

The Erguna block is an important part of the Greater Hinggan Mountains volcanic plutonic belt. In order to obtain a more reasonable interpretation on the tectonic setting of Erguna Block, we should consider the question from a larger scale. Early Cretaceous magmatic activity in NE China was divided into two stages, early Cretaceous (145–138 Ma) and late Early Cretaceous (~120–105 Ma) (Wang et al., 2014; Tang et al., 2015; Guo et al., 2018; Mao, 2020). Magmatism in the late Early Cretaceous was widely developed in the Greater Hinggan Mountains, Songliao Basin and the eastern part of Jilin and Heilongjiang (Mao 2020). The late Early Cretaceous magmatic rocks in the eastern part of Jilin and Heilongjiang belong to a low-to medium-K calc-alkaline series (Figure 6C), which formed in an active continental margin setting related to the subduction of the Paleo-Pacific Plate beneath the Eurasian continent (Xu et al., 2013; Tang et al., 2015; Guo et al., 2018; Mao, 2020). Magmatic rocks in the Greater Hinggan Mountains and the Songliao Basin are classified as high-K calc-alkaline series (Figure 6C; Guo et al., 2018; Mao, 2020) and a bimodal volcanic rock, suggests that those magmatic rocks occurred in an extensional environment related to either to a back arc setting or to delamination of a thickened crust, or both (Xu et al., 2013; Tang et al., 2015; Tang et al., 2016b). The early Cretaceous magmatic rocks only occur in the west of Songliao Basin, are mainly distributed in the Great Hinggan Mountains (Xu et al., 2008; Meng et al., 2011; Xu et al., 2011; Ji et al., 2019), indicating that this magmatic activity should be attributed to the influence of the Mongol–Okhotsk suture belt. Those magmatic rocks include alkali feldspar granite, syenogranite, monzogranite, granodiorite, trachyte, and rhyolite (Figures 6A,B; Guo et al., 2019), belong chemically to a high-K calc-alkaline series, combined with the presence of A-type rhyolites within the coeval Jixiangfeng Formation in the Erguna Massif, suggests that the early Cretaceous magmatism formed in an extensional environment (Meng et al., 2011; Xu et al., 2011). The widely dispersed metamorphic core complexes in eastern China, Mongol, and the outer Baikal area of Russia also significantly supported the extensional environment of the Great Hinggan Mountains in the early Cretaceous (Zorin, 1999; Wang et al., 2011). Therefore, the early Cretaceous magmatic activities in the Great Hinggan Mountains were formed in the extensional environment after the closure of the Mongol-Okhotsk Ocean (Wang et al., 2012; Xu et al., 2013; Tang et al., 2015; Liu et al., 2019). According to the above conclusions, and considering the diagenetic and metallogenic age and geochemical features of alkali-feldspar granites, we believe that the Shanagan hydrothermal vein-type Mo deposit was formed in the extensional environment after the closure of the Mongol-Okhotsk Ocean.

# 7 Conclusion

Based on geochronology, and geochemistry of the Shanagen hydrothermal vein-type Mo deposit, we have come to the following conclusions:

(1) The alkali-feldspar granite was emplaced at 144.7 ± 0.7 Ma, and the mineralization of the Shanagen hydrothermal vein-type Mo deposit was 143.1 ± 3.8 Ma. Both were formed in the early Cretaceous.
(2) The alkali-feldspar granite from the Shanagen hydrothermal vein-type Mo deposit belong to highly differentiated I-type granite, which was formed from magma generated by partial melting of lower crust.
(3) The Shanagen hydrothermal vein-type Mo deposit was formed in the extensional environment after the closure of the Mongol-Okhotsk Ocean.

## Data availability statement

The original contributions presented in the study are included in the article/supplementary material, further inquiries can be directed to the corresponding author.

## Author contributions

Conceptualization, YL; methodology, YW and YL; field work and investigation, YW, YL, AL, LT, and YY; data curation, YW and AL; writing—original draft preparation, YW and YL All authors have read and agreed to the published version of the manuscript.

## Funding

This work is funded by the Opening Foundation of Hebei Key Laboratory of Strategic Critical Mineral Resource (HGU-RGM2046).

## Acknowledgments

We are very grateful to the Hebei Key Laboratory of Strategic Critical Mineral Resource for its support on the data analysis.

## Conflict of interest

The authors declare that the research was conducted in the absence of any commercial or financial relationships that could be construed as a potential conflict of interest.

## Publisher's note



## References

Arzhannikova, A. V., Demonterova, E. I., Jolivet, M., Mikheeva, E. A., Ivanov, A. V., Arzhannikov, S. G., et al. (2022). Segmental closure of the Mongol-Okhotsk ocean: Insight from detrital geochronology in the east transbaikalia basin. *Geosci. Front.* 13, 101254. doi:10.1016/j.gsf.2021.101254

Bea, F., Mazhari, A., Montero, P., Amini, S., and Ghalamghash, J. (2011). Zircon dating, Sr and Nd isotopes, and element geochemistry of the khalifan pluton, NW Iran: Evidence for variscan magmatism in a supposedly cimmerian superterrane. *J. Asian Earth Sci.* 40, 172–179. doi:10.1016/j.jseaes.2010.08.005

Boynton, W. V. (1984). "Geochemistry of the rare Earth elements, meteorite studies," in *Rare earth element geochemistry*. Editor P. Henderson (Amsterdam: Elsevier), 63–114.

Cao, Y. H., and Liu, Y. F. (2020). Zircon U–Pb age, geochemical characteristics and metallogenic significance of ore–bearing porphyry of the Jiawula Ag–Pb–Zn deposit in Inner Mongolia. *Geol. Bull. China* 39, 353–364.

Chappell, B. W. (1999). Aluminium saturation in I- and S-type granites and the characterization of fractionated haplogranites. *Lithos* 46, 535–551. doi:10.1016/s0024-4937(98)00086-3

Chappell, B. W., and White, A. J. R. (1992). I- and S-type granites in the lachlan fold belt. *Trans. R. Soc. Edinb. Earth Sci.* 83, 1–26. doi:10.1130/SPE272-p1

Chen, Z. G. (2010). *Mesozoic tectonic–magmatic mineralization of Derbugan metallogenic belt in NE China, and its geodynamic setting*. Beijing, China: Dissertation, Institute of Geology and Geophysics, Chinese Academy of Sciences, 1–193.

Chen, Z. G., Zhang, L. C., Lu, B. Z., Li, Z. L., Wu, H. Y., Xiang, P., et al. (2010). Geochronology and geochemistry of the Taipingchuan copper-molybdenum deposit in Inner Mongolia, and its geological significances. *Acta Petrol. Sin.* 26, 1437–1449.

Chen, Z. G., Zhang, L. C., and Wan, B. (2006). Geological setting and metallogenic prognosis of the De'erbugan polymetallic belt in the Da Hinggan Mountains. *Mineral. Deposits* 25, 11–14.

Chen, Z. G., Zhang, L. C., Wan, B., Wu, H. Y., and Cleven, N. (2011). Geochronology and geochemistry of the Wunugetushan porphyry Cu–Mo deposit in NE China, and their geological significance. *Ore Geol. Rev.* 43, 92–105. doi:10.1016/j.oregeorev.2011.08.007

Cogné, J. P., Kravchinsky, V. A., Halim, N., and Hankard, F. (2005). Late jurassic-early cretaceous closure of the Mongol-Okhotsk ocean demonstrated by new mesozoic palaeomagnetic results from the trans-baïkal area (SE siberia). *Geophys. J. Int.* 163, 813–832. doi:10.1111/j.1365-246X.2005.02782.x

Deng, J. F., Xiao, Q. H., Su, S. G., Liu, C., Zhao, G. C., Wu, Z. X., et al. (2007). Igneous petrotectonic assemblages and tectonic settings: A discussion. *Geol. J. China Univ.* 13, 392–402.

Deng, X. H., Li, W. B., and Li, N. (2009). Fluid inclusion constraints on the origin of zhifang Mo deposit songxian county, henan province. *Acta Petrol. Sin.* 24, 2133–2148.

Domeier, M., and Torsvik, T. H. (2014). Plate tectonics in the late Paleozoic. *Geosci. Front.* 5, 303–350. doi:10.1016/j.gsf.2014.01.002

Dong, G. C., Mo, X. X., Zhao, Z. D., Zhu, D. C., Goodman, R. C., Kong, H. L., et al. (2013). Zircon U–Pb dating and the petrological and geochemical constraints on lincang granite in western yunnan, China: Implications for the closure of the paleo-tethys ocean. *J. Asian Earth Sci.* 62, 282–294. doi:10.1016/j.jseaes.2012.10.003

Dong, P. P., Li, Y. J., Wang, G. H., Xin, H. T., Wang, J. F., Li, H. Y., et al. (2020). Geological and chronological characteristics of the baiyin' gaolao Formation in gaoyaowula, inner Mongolia. *J. Geomechanics* 27, 135–152.

Fan, W. M., Guo, F., Wang, Y. J., and Lin, G. (2003). Late Mesozoic calc–Alkaline volcanism of post-orogenic extension in the northern Da Hinggan Mountains, northeastern China. *J. Volcanol. Geotherm. Res.* 121, 115–135. doi:10.1016/S0377-0273(02)00415-8

Fritzell, E. H., Bull, A. L., and Shephard, G. E. (2016). Closure of the Mongol-Okhotsk Ocean: Insights from seismic tomography and numerical modelling. *Earth Planet. Sci. Lett.* 445, 1–12. doi:10.1016/j.epsl.2016.03.042

Fu, Q., Ge, W. S., Wen, C. S., and Li, S. B. (2014). Geochemistry and Genesis of youmapo W-Mo deposit in guangxi. *Ore Depos. Geol.* 33, 785–794.

Gao, B. Y., Zhang, L. C., Jin, X. D., Li, W. J., Chen, Z. G., and Zhu, M. T. (2016). Geochronology and geochemistry of the Badaguan porphyry Cu–Mo deposit in Derbugan metallogenic belt of the NE China, and their geological significances. *Int. J. Earth Sci.* 105, 507–519. doi:10.1007/s00531-015-1261-4

Ge, W. C., Chen, J. S., Yang, H., Zhao, G. C., Zhang, Y. L., and Tian, D. X. (2015). Tectonic implications of new zircon U–Pb ages for the Xinghuadukou complex, Erguna massif, northern Great xing'an range, NE China-Pb ages for the Xinghuadukou complex, Erguna massif, northern Great xing'an range, NE China. *J. Asian Earth Sci.* 106, 169–185. doi:10.1016/j.jseaes.2015.03.011

Ge, W. C., Wu, F. Y., Zhou, C. Y., and Zhang, J. H. (2007). Metallogenic epoch and geodynamic significance of porphyry Cu, Mo deposits in the eastern Xingmeng orogenic belt. *Chin. Sci. Bull.* 52, 2407–2417.

Gou, J., Sun, D. Y., Ren, Y. S., Liu, S. Y., Zhang, C. L., Fu, T. H., et al. (2013). Petrogenesis and geodynamic setting of neoproterozoic and late paleozoic

magmatism in the manzhouli–erguna area of inner Mongolia, China: Geochronological, geochemical and Hf isotopic evidence. *J. Asian Earth Sci.* 67 (68), 114–137. doi:10.1016/j.jseaes.2013.02.016

Guo, J., Sun, D. Y., and Zhen, Q. (2018). Late jurassic–early cretaceous tectonic evolution of the Great xing'an range: Geochronological and geochemical evidence from granitoids and volcanic rocks in the Erguna block, NE China. *Int. Geol. Rev.* 61, 1842–1863. doi:10.1080/00206814.2018.1561336

Guo, Z. J., Li, J. W., Xu, X. Y., Song, Z. Y., Dong, X. Z., Tian, J., et al. (2016). Sm-Nd dating and REE Composition of scheelite for the Honghuaerji scheelite deposit, Inner Mongolia, Northeast China. *Lithos* 261, 307–321. doi:10.1016/j.lithos.2016.03.006

Harrison, T. M., and Watson, E. B. (1984). The behavior of apatite during crustal anatexis-Equilibrium and kinetic considerations. *Geochim. Cosmochim. Acta* 48, 1467–1477. doi:10.1016/0016-7037(84)90403-4

Hoskin, P. W. O., and Schaltegger, U. (2003). The composition of zircon and igneous and metamorphic petrogenesis. *Rev. Mineral. Geochem.* 53, 27–62. doi:10.2113/0530027

Huang, S. Q., Dong, S. W., Hu, J. M., Shi, W., Chen, X. H., and Liu, Z. Q. (2016). the formation and tectonic evolution of the mongol-okhotsk belt. *Acta Geol. Sin.* 90, 2192–2205.

Hui, K., Qin, K. Z., Li, Z. Z., Wang, F. Y., Gao, S., Han, R., et al. (2021). The linkage between the Jiawula–Chaganbulagen Ag–Pb–Zn and adjacent porphyry Mo–Cu mineralization, Inner Mongolia, northeast China. *Ore Geol. Rev.* 134, 104153. doi:10.1016/j.oregeorev.2021.104153

IMBGMR (Inner Mongolian Bureau of Geology Mineral Resources) (1996). *Lithostratigraphy of inner Mongolia*. Wuhan: China University of Geosciences Press, 1–342.

IMBGMR (Inner Mongolian Bureau of Geology Mineral Resources) (1991). *Regional geology of inner Mongolia*, 1. Beijing: Geological Publishing House.

Irber, W. (1999). The lanthanide tetrad effect and its correlation with K/Rb, Eu/Eu*, Sr/Eu, Y/Ho, and Zr/Hf of evolving peraluminous granite suites. *Geochimica Cosmochimica Acta* 63, 489–508. doi:10.1016/S0016-7037(99)00027-7

Ji, D., Liu, H. C., and Li, Y. L. (2019). Large-scale early cretaceous lower-crust melting derived adakitic rocks in NE China: Implications for convergent bidirectional subduction and slab rollback. *Int. Geol. Rev.* 6, 2324–2343. doi:10.1080/00206814.2019.1697968

Kang, Y. J., Wang, Y. J., Huang, G. J., She, H. Q., Xiang, A. P., Tian, J., et al. (2014). Study of rock–forming and ore–forming ages of Badaguan prophypy Cu–Mo deposit in Inner Mongolia. *Mineral. Deposits* 33, 795–806.

Koval, P. V., Grebenshchikova, V. I., Lustenberg, E. E., and Henney, P. J. (1999). Database of granites in the Mongol–Okhotsk zone, Mongolia–Siberia, and its use in mineral exploration. *J. Geochem. Explor.* 66, 199–210. doi:10.1016/S0375-6742(99)00040-0

Kravchinsky, V. A., Cogné, J., Harbert, W. P., and Kuzmin, M. I. (2002). Evolution of the Mongol–Okhotsk ocean as constrained by new palaeomagnetic data from the mongol–okhotsk suture zone, siberia. *Geophys. J. Int.* 148, 34–57. doi:10.1046/j.1365-246X.2002.01557.x

Le Maitre, R. W. (2002). *Igneous rocks: A classification and glossary of terms*. 2nd edition. Cambridge: Cambridge University Press, 33–39.

Li, C. F., Liu, Z. J., Mi, K. F., Wang, J. P., Liu, R. B., Zou, J. Y., et al. (2014). Metallogenic age and ore Genesis of the Badaguan porphyry copper–molybdenum deposit in Inner Mongolia. *Geol. China* 41, 1253–1269.

Li, C., Qu, W. J., and Du, A. D. (2009). Comprehensive study on extraction of Rhenium with acetone in Re–Os isotopic dating. *Rock Mineral Analysis* 28, 233–238.

Li, C., Qu, W. J., Zhou, L. M., and Du, A. D. (2010). Rapid separation of osmium by direct distillation with Carius tube. *Rock Mineral Analysis* 29, 14–16.

Li, C., Yang, X., Zhao, H., Zhou, L. M., Du, A. D., Li, X. W., et al. (2015). High precise isotopic measurements of pg-ng Os by negative ion thermal ionization mass spectrometry. *Rock Mineral Analysis* 34, 392–398.

Li, T. G. (2016). *Metallogenesis of the Jiawula- chaganbulagen Pb-Zn-Ag orefield, inner Mongolia*. China. Dissertation. Beijing, China: China University of Geosciences.

Li, T. G., Wu, G., Liu, J., Hu, Y. Q., Zhang, Y. F., and Luo, D. F. (2014). Rb-Sr isochron age of the Jiawula Pb-Zn-Ag deposit in the Manzhouli area and its geological significance. *Acta Petrol. Sin.* 30, 257–270.

Li, T. G., Wu, G., Liu, J., Wang, G. R., Hu, Y. Q., Zhang, Y. F., et al. (2016). Geochronology, fluid inclusions and isotopic characteristics of the Chaganbulagen Pb–Zn–Ag deposit, Inner Mongolia, China. *Lithos* 261, 340–355. doi:10.1016/j.lithos.2016.04.029

Li, Y., Ding, L. L., Xu, W. L., Wang, F., Tang, J., Zhao, S., et al. (2015). Geochronology and geochemistry of muscovite granite in Sunwu area, NE China: Implications for the timing of closure of the Mongol-Okhotsk Ocean. *Acta Petrol. Sin.* 31, 56–66.

Li, Y. L., Liu, H. C., Huangfu, P. P., He, H. Y., and Liu, Y. Z. (2018). Early cretaceous lower crustal reworking in NE China: Insights from geochronology and geochemistry of felsic igneous rocks from the Great xing'an range. *Int. J. Earth Sci.* 107, 1955–1974. doi:10.1007/s00531-017-1581-7

Liang, X. L., Sun, J. G., and Qiu, D. M. (2020). Genesis of biliya valley Ag-Pb-Zn polymetallic deposit on Western slope of Great xing'an rang. *J. Jilin Univ. (Earth Sci. Ed.* 50, 781–799.

Liu, H. C., Li, Y. L., He, H. Y., Huangfu, P. P., and Liu, Y. Z. (2018). Two-phase southward subduction of the Mongol-Okhotsk oceanic plate constrained by Permian-Jurassic granitoids in the Erguna and Xing'an massifs (NE China). *Lithos* 304, 347–361. doi:10.1016/j.lithos.2018.01.016

Liu, H. C., Li, Y. L., Wu, L. W., Huangfu, P. P., and Zhang, M. (2019). Geochemistry of high-Nb basalt-andesite in the Erguna Massif (NE China) and implications for the early Cretaceous back-arc extension. *Geol. J.* 54, 291–307. doi:10.1002/gj.3176

Liu, H. C., Shao, J., Zhu, G. Y., and Li, Y. L. (2021). Neoarchean basement, mantle enrichment and crustal extraction in central asia: Petrogenesis of 2.5 Ga amphibolite and metadiorite in NE China. *Am. J. Sci.* 321, 1350–1379. doi:10.2475/09.2021.03

Liu, Y. H., Liu, W., Liu, A. R., Tian, Y., Tian, N., and Liu, Z. H. (2014). Geological characteristics and prospecting potential of shanagenhuduge molybdenum deposits, xinbaerhuyouqi, inner Mongolia. *Geol. Sci. Technol. Inf.* 33, 149–155.

Liu, Y. S., Hu, Z. C., Zong, K. Q., Gao, C. G., Gao, S., Xu, J., et al. (2010). Reappraisement and refinement of zircon U-Pb isotope and trace element analyses by LA-ICP-MS. *Chin. Sci. Bull.* 55, 1535–1546. doi:10.1007/s11434-010-3052-4

Lü, X. B., Yang, J. S., and Fang, X. J. (2020). Geology and genesis of lead-zinc polymetallic deposits in the Great xing'an range. *Earth Sci.* 45, 4399–4427.

Ludwig, K. R. (2003). *Isoplot/ex, version 3: A geochronological toolkit for microsoft excel: Berkeley*. Berkeley, CA: Geochronology Centre.

Maniar, P., and Piccoli, P. (1989). Tectonic discrimination of granitoids. *Geol. Soc. Am. Bull.* 5, 635–643. doi:10.1130/0016-7606(1989)101<0635:tdog>2.3.co;2

Mao, A. Q. (2020). *Magmatic rocks of Mesozoic volcanic basins in central Erguna Block: Petrogenesis and geodynamics*. Jilin, China: Dissertation, Jilin University, 1–186.

Meng, E., Xu, W. L., Yang, D. B., Qiu, K. F., Li, C. H., and Zhu, H. T. (2011). Zircon U-Pb chronology, geochemistry of Mesozoic volcanic rocks from the Lingquan basin in Manzhouli area, and its tectonic implications. *Acta Petrol. Sin.* 27, 1209–1226.

Metelkin, D. V., Gordienko, I. V., and Klimuk, V. S. (2007). Paleomagnetism of upper jurassic basalts from transbaikalia: New data on the time of closure of the Mongol-Okhotsk ocean and mesozoic intraplate tectonics of central asia. *Russ. Geol. Geophys.* 48, 825–834. doi:10.1016/j.rgg.2007.09.004

Mi, K. F., Lu, Z. C., Liu, Z. J., Yu, X. F., and Yan, T. F. (2021). Compositions of Cu and Mo isotopes, sericite Ar-Ar ages of Wunugtushan Cu-Mo deposit in Inner Mongolia: Implications for regional mineralization. *Acta petrol. Sin.* 37, 1785–1798. doi:10.18654/1000-0569/2021.06.09

Mi, K. F., Liu, Z. J., Liu, R. B., Li, C. F., Wang, J. P., and Peng, R. M. (2018). U-Pb zircon, geochemical and Sr-Nd-Hf isotopic constraints on age and origin of the intrusions from wunugetushan porphyry deposit, northeast China: Implication for triassic-jurassic Cu-Mo mineralization in Mongolia-Erguna metallogenic belt. *Int. Geol. Rev.* 60, 496–512. doi:10.1080/00206814.2017.1347531

Niu, S. D., Li, S. R., Huizenga, J. M., Santosh, M., Zhang, D. H., Zeng, Y. J., et al. (2017). Zircon U-Pb geochronology and geochemistry of the intrusions associated with the Jiawula Ag-Pb-Zn deposit in the Great Xing'an Range, NE China and their implications for mineralization. *Ore Geol. Rev.* 86, 35–54. doi:10.1016/j.oregeorev.2017.02.007

Nie, F. J., Liu, Y., Liu, Y. F., Jiang, S. H., Zhang, K., and Liu, Y. (2011). Ore-forming Processes of Siliver-Polymetallic deposits occurring within Tsav-Jiawul region along China-Mongolian border. *J. Jilin Univ. (Earth Sci. Ed.* 41, 1715–1725.

Niu, S. D., Li, S. R., Santosh, M., Zhang, D. H., Li, Z. D., Shan, M. J., et al. (2016). Mineralogical and isotopic studies of base metal sulfides from the Jiawula Ag–Pb–Zn deposit, Inner Mongolia, NE China. *J. Asian Earth Sci.* 115, 480–491. doi:10.1016/j.jseaes.2015.10.020

Patiño Douce, A. E. (1999). "What do experiments tell us about relative contributions of crust and mantle to the origin of granitic magmas?," in *Understanding granites: Integrating new and classical techniques*. Editor A. Castro, et al. (London: Geological Society, London, Special Publication), 55–75.

Peccerillo, A., and Taylor, A. R. (1976). Geochemistry of Eocene calc-alkaline volcanic rocks from the Kastamonu area, Northern Turkey. *Contr. Mineral. Petrol.* 58, 63–81. doi:10.1007/BF00384745

Richards, J. P. (2011). Magmatic to hydrothermal metal fluxes in convergent and collided margins. *Ore Geol. Rev.* 40, 1–26. doi:10.1016/j.oregeorev.2011.05.006

Shao, Y. J., Li, G. Z., Jiang, H. J., Xu, C., Kou, S., Lian, C. Q., et al. (2020). LA-ICP-MS zircon U-Pb age and geochemistry of volcanic rocks from Manitu Formation in Hanbumiao area, the Western Great Xing'an Range and their tectonic significance. *Acta Geol. Sin.* 94, 3590–3606.

She, H. Q., Li, J. W., Xiang, A. P., Guan, J. D., Zhang, D. Q., Yang, Y. C., et al. (2012). U-Pb ages of the zircons from primary rocks in middle-northern Daxinganling and its implications to geotectonic evolution. *Acta Petrol. Sin.* 28, 571–594.

Smoliar, M. L., Walker, R. J., and Morgan, J. W. (1996). Re-Os ages of Group IIA, IIIA, IVA, and IVB iron meteorites. *Science* 271, 1099–1102. doi:10.1126/science.271.5252.1099

Streckeisen, A., and Le Maitre, R. W. (1979). A chemical approximation to the modal QAPF classification of the igneous rocks. *Neues Jahrb. für Mineral. Abt.* 136, 169–206.

Sun, D. Y., Gou, J., Ren, Y. S., and Liu, X. (2011). Zircon U-Pb dating and study on geochemistry of volcanic rocks in Manitu Formation from southern Manchuria, Inner Mongolia. *Acta Petrol. Sin.* 27, 3083–3094.

Sun, D. Y., Guo, J., Wang, T. H., Ren, Y. S., Liu, Y. J., Guo, H. Y., et al. (2013). Geochronological and geochemical constraints on the Erguna massif basement, NE China–subduction history of the Mongol–Okhotsk oceanic crust. *Int. Geol. Rev.* 55, 1801–1816. doi:10.1080/00206814.2013.804664

Sun, L. X., Ren, B. F., Zhao, F. Q., Ji, S. P., and Geng, J. Z. (2013). Late paleoproterozoic magmatic records in the eerguna massif: Evidences from the zircon U–Pb dating of granitic gneisses. *Geol. Bull. China* 32, 341–352.

Sun, S. S., and Mcdonough, W. F. (1989). "Chemical and isotopic systematics of ocean basins: Implications for mantle composition and processes," in *Magmatism in ocean basins*. Editors A. D. Saunders and M. J. Norry (London: Geological Society of London and Blackwell Scientific Publications), 313–345.

Sylvester, P. J. (1998). Post-collisional strongly peraluminous granites. *Lithos* 45, 29–44. doi:10.1016/S0024-4937(98)00024-3

Tan, H. Y., He, Z. H., and Chen, F. (2017). Zircon U-Pb ages and geochemical characteristics of volcanic rocks in Baiyingaolao Formation of Suolun area within central Da Hinggan Mountains and their tectonic implications. *Geol. Bull. China* 36, 893–908.

Tang, J., Xu, W. L., and Wang, F. (2016b). Rock associations and their spatial-temporal variations of the early mesozoic igneous rocks in the NE asia: Constraints on the initial subduction timing of the Paleo-Pacific plate. *Bull. Mineralogy, Petrology Geochem.* 35, 1181–1194.

Tang, J., Xu, W. L., Wang, F., Wang, W., Xu, M. J., and Zhang, Y. H. (2014). Geochronology and geochemistry of early–middle triassic magmatism in the Erguna massif, NE China: Constraints on the tectonic evolution of the Mongol–Okhotsk ocean. *Lithos* 184, 1–16. doi:10.1016/j.lithos.2013.10.024

Tang, J., Xu, W. L., Wang, F., Wei, W., Xu, M. J., and Zhang, Y. H. (2013). Geochronology and geochemistry of neoproterozoic magmatism in the Erguna massif, NE China: Petrogenesis and implications for the breakup of the rodinia supercontinent. *Precambrian Res.* 224, 597–611. doi:10.1016/j.precamres.2012.10.019

Tang, J., Xu, W. L., Wang, F., Zhao, S., and Li, Y. (2016a). Early Mesozoic southward subduction history of the Mongol–Okhotsk oceanic plate: Evidence from geochronology and geochemistry of Early Mesozoic intrusive rocks in the Erguna Massif, NE China. *Gondwana Res.* 31, 218–240. doi:10.1016/j.gr.2014.12.010

Tang, J., Xu, W. L., Wang, F., Zhao, S., and Li, Y. (2015). Geochronology, geochemistry, and deformation history of late jurassic–early cretaceous intrusive rocks in the Erguna massif, NE China: Constraints on the late mesozoic tectonic evolution of the mongol–okhotsk orogenic belt. *Tectonophysics* 658, 91–110. doi:10.1016/j.tecto.2015.07.012

Tomurtogoo, O., Windley, B. F., Kroner, A., Badarch, G., and Liu, D. Y. (2005). Zircon age and occurrence of the adaatsag ophiolite and muron shear zone, central Mongolia: Constraints on the evolution of the Mongol-Okhotsk ocean, suture and orogen. *J. Geol. Soc. Lond.* 162, 125–134. doi:10.1144/0016-764903-146

Van, R., Van, D. J. J., Domeier, M., Spakman, W., and Torsvik, T. H. (2015). Latest jurassic–earliest cretaceous closure of the Mongol-Okhotsk ocean: A paleomagnetic and seismological-tomographic analysis. *Geol. Soc. Am. Special Pap.*, 589–606. doi:10.1130/2015.2513(19)

Wang, J. F., Li, Y. J., Li, H. Y., and Dong, P. (2019). Post-orogeny of the Hegenshan suture zone: Zircon U- Pb age and geochemical constraints from volcanic rocks of the Manketouebo Formation. *Geol. Bull. China* 38, 1443–1454.

Wang, J. X., Xu, J., Yu, H., Shu, G. L., Feng, D. S., and Shi, J. M. (2019). Geological characteristics and metallogenic age of the large silver–lead–zinc deposit in halasheng of manzhouli area, inner Mongolia. *Geol. Resour.* 28, 18–23.

Wang, T., Guo, L., Zhang, L., Yang, Q. D., Zhang, J. J., Tong, Y., et al. (2015). Timing and evolution of Jurassic–Cretaceous granitoid magmatisms in the Mongol–Okhotsk belt and adjacent areas, NE Asia: Implications for transition from contractional crustal thickening to extensional thinning and geodynamic settings. *J. Asian Earth Sci.* 97, 365–392. doi:10.1016/j.jseaes.2014.10.005

Wang, T. H., Zhang, S. Y., Sun, D. Y., Gou, J., Ren, Y. S., Wu, P. F., et al. (2014). Zircon U–Pb ages and Hf isotopic characteristics of Mesozoic granitoids from southern Manzhouli, Inner Mongolia. *Glob. Geol.* 33, 26–38.

Wang, T., Tong, Y., Xiao, W. J., Guo, L., Windley, B. F., Donskaya, T., et al. (2022a). Rollback, scissor-like closure of the Mongol-Okhotsk ocean and formation of an orocline: Magmatic migration based on a large archive of age-data. *Natl. Sci. Rev.* 9, nwab210. doi:10.1093/nsr/nwab210

Wang, T., Zheng, Y. D., Zhang, J. J., Zeng, L. S., Donskaya, T., Guo, L., et al. (2011). Pattern and kinematic polarity of late Mesozoic extension in continental NE Asia: Perspectives from metamorphic core complexes. *Tectonics* 30, 1–27. doi:10.1029/2011tc002896

Wang, W., Xu, W. L., Wang, F., and Meng, E. (2012). Zircon U–Pb chronology and assemblages of mesozoic granitoids in the manzhouli–erguna area, NE China: Constraints on the regional tectonic evolution. *Geol. J. China Univ.* 18, 88–105.

Wang, Y. H., Zhao, C. B., Zhang, F. F., Liu, J. J., Wang, J. P., Peng, R. M., et al. (2015). SIMS zircon U-Pb and molybdenite Re-Os geochronology, Hf isotope, and whole-rock geochemistry of the Wunugetushan porphyry Cu-Mo deposit and granitoids in NE China and their geological significance. *Gondwana Res.* 28, 1228–1245. doi:10.1016/j.gr.2014.10.001

Wang, Z. L., Li, Z. L., and Zheng, X. M. (2017). Petrogeochemistry, records of hydrothermal activities and geochronology of the Taipingchuan Mo-Cu Deposi, tInner Mongolia. *Resour. Geol. Surv.* 8, 184–195.

Wang, Z. W., Wang, Z. H., Zhang, Y. J., Xu, B., Li, Y. G., Tian, Y. J., et al. (2022b). Linking ~1.4–0.8 Ga volcano-sedimentary records in eastern Central Asian orogenic belt with southern Laurentia in supercontinent cycles. *Gondwana Res.* 105, 416–431. doi:10.1016/j.gr.2021.09.019

Wang, Z. W. Zhu, T. C. Yu J. W., and Yuan, L. L. (2022c). *Forming proterozoic basement within eastern central asian orogenic belt: Evidence from zircon U-Pb-Hf-O isotopes*. Journal of Central South University. doi:10.1007/s11771-022-5094-6

Wang, X., Duan, M. X., Ren, Y. S., Hou, Z. S., Sun, D. Y., and Hao, Y. J. (2016). Characteristics of fluid inclusion and minimization age of Badaguan Cu–Mo deposit in Erguna Area, Inner Mongolia. *J. Jilin Univ. (Earth Sci. Ed.)* 46, 1354–1367.

Wu, F. Y., Li, X. H., Yang, J. H., and Zheng, Y. (2007). Log structures on generalized semi-stable varieties. *Acta Math. Sin. Engl. Ser.* 26, 1217–1232. doi:10.1007/s10114-005-0854-4

Wu, F. Y., Jahn, B. M., Wilde, S. A., Lo, C. H., Yui, T. F., Lin, Q., et al. (2003). Highly fractionated I-type granites in NE China (I): Geochronology and petrogenesis. *Lithos* 66, 241–273. doi:10.1016/s0024-4937(02)00222-0

Wu, G., Chen, Y. C., Chen, Y. J., and Zeng, Q. T. (2012). Zircon U–Pb ages of the metamorphic supracrustal rocks of the Xinghuadukou Group and granitic complexes in the Argun massif of the northern Great Hinggan Range, NE China, and their tectonic implications. *J. Asian Earth Sci.* 49, 214–233. doi:10.1016/j.jseaes.2011.11.023

Wu, G., Wang, G. R., Liu, J., Zhou, Z. H., Li, T. G., and Wu, H. (2014). Metallogenic series and ore-forming pedigree of main ore deposits in northern Great Xing'an Range. *Mineral. Deposits* 33, 1127–1150.

Wu, H., Chen, M., Gong, Q. D., Cao, Y. B., Zhang, L. Q., Liu, X. Y., et al. (2019). Study of geochronology and geochemistry of volcanic rocks from Meiletu Formation in horqin right wing front banner, inner Mongolia. *Geol. Bull. China* 38, 1836–1845.

Xu, L. Q., Liu, C., Deng, J. F., Li, N., Dai, M., and Bai, L. B. (2014). Geochemical characteristics and zircon U-Pb SHRIMP age of igneous rocks in Erentaolegai silver deposit, Inner Mongolia. *Acta Petrol. Sin.* 30, 3203–3212.

Xu, M. J., Xu, W. L., Meng, E., and Wang, F. (2011). LA-ICP-MS zircon U-Pb chronology and geochemistry of Mesozoic volcanic rocks from the Shanghulin-Xiangyang basin in Ergun area, northeastern Inner Mongolia. *Geol. Bull. China* 30, 1321–1338.

Xu, W. L., Ge, W. C., and Pei, F. P. (2008). Chronological framework of Mesozoic volcanism in Northeast China and its tectonic significance. *Bull. Mineralogy, Petrology Geochem.* 27, 286–287.

Xu, W. L., Pei, F. P., Wang, F., Meng, E., Ji, W. Q., Yang, D. B., et al. (2013). Spatial–temporal relationships of mesozoic volcanic rocks in NE China: Constraints on tectonic overprinting and transformations between multiple tectonic regimes. *J. Asian Earth Sci.* 74, 167–193. doi:10.1016/j.jseaes.2013.04.003

Xu, Z. T., Liu, Y., Sun, J. G., Liang, X. L., and Xu, Z. K. (2020). Nature and ore formation of the erdaohezi Pb–Zn deposit in the Great xing'an range, NE China. *Ore Geol. Rev.* 119, 103385. doi:10.1016/j.oregeorev.2020.103385

Yang, H. X., Gao, L. D., Gao, Y. S., Sui, H. T., Zhao, Z. F., Lv, J., et al. (2019). Zircon U-Pb age and geochemistry of the stratotype section of the Meiletu Formation in middle southern Da Hinggan Mountains and its geological significance. *Geol. Bull. China* 38, 845–857.

Yang, Y. C., Guo, W. J., Wang, Y. J., She, H. Q., Li, J. W., and Zhang, B. (2015). Rb-Sr dating of sphalerites from Dongjun Pb-Zn-Ag deposit, Inner Mongolia and its geological significance. *Earth Sci. Front.* 22, 348–356. doi:10.13745/j.esf.2015.03.030

Yang, Y. J., Yang, X. P., Jiang, B., Wang, Y., and Pang, X. J. (2022). Spatio-temporal distribution of mesozoic volcanic strata in the Great xing'an range: Response to subduction of the Mongol-Okhotsk ocean and paleo-pacific ocean. *Earth Sci. Fontiers* 29, 115–131.

Yang, Z. L., Zhang, D. Q., Li, J. W., She, H. Q., Feng, C. Y., and Dong, Y. J. (2009). Ore-forming types, metallogenic zoning and potential prospecting areas in Southwestern sector of Derbugan metallogenic bel. *Mineral. Deposits* 28, 53–62.

Yin, Z. G., Hao, K., Liu, C. H., Wang, Y., Li, H. N., Li, M., et al. (2019). Geochronological and geochemical characteristics of rhyolite in the manketou'ebo Formation of Dong ujimqin banner, inner Mongolia, and its geological implications. *Geol. Bull. China* 38, 1825–1835.

Yuan, Y., An, F., and Chen, Bo. (2020). A review of the research status of geoIogicaI and geochemicaI characteristics of quartz vein-type moIybdenum deposits. *Chin. J. Geol.* 55, 598–614.

Zeng, Q. D., Liu, J. M., Zhang, Z. L., Chu, S. X., Wang, Y. B., Duan, X. X., et al. (2009). Mineralizing types, geological characteristics and geodynamic background of molybdenum deposits in Xilamulun molybdenum polymetal metallogenic belt on northern margin of North China Craton. *Acta Petrol. Sin.* 25, 1225–1238.

Zhang, L. C., Chen, Z. G., Wu, H. Y., Xiang, P., and Huang, S. W. (2010). Tectonic magmatic mineralization and dynamic setting of Derbugan polymetallic metallogenic belt in Mongolia Okhotsk orogenic belt. *Mineral. Deposits* 29, 125–126.

Zhang, L. C., Gao, B. Y., Li, W. J., Chen, Z. G., Sakyi, P. A., and Jin, X. D. (2014). Early mesozoic tectono-magmatic activity and mineralization in Northeast China: Evidence from Re-Os to U-Pb studies of the taipingchuan porphyry Cu-Mo deposit in the derbugan metallogenic belt. *Int. Geol. Rev.* 56, 1837–1851. doi:10.1080/00206814.2014.963709

Zhang, S. H., Zhao, Y., Davis, G. A., Ye, H., and Wu, F. (2014). Temporal and spatial variations of mesozoic magmatism and deformation in the north China craton: Implications for lithospheric thinning and decratonization. *Earth. Sci. Rev.* 131, 49–87. doi:10.1016/j.earscirev.2013.12.004

Zhao, Y., Lu, J. C., Zhang, D. B., Zhou, Y. H., Shao, J., and Wang, B. (2017). Rb–Sr isochron age of Derbur Pb–Zn–Ag deposit in Erguna massif of northeast Inner Mongolia and its geological significance. *Mineral. Deposits* 36, 893–904.

Zhu, Q., Wu, G., Zhang, J. F., Shao, J., and Zhu, H. C. (2001). Research Progress on metallogenic zoning and exploration technology of Derbugan metallogenic belt. *Chin. Geol.* 28, 19–27.

Zorin, Y. A. (1999). Geodynamics of the Western part of the Mongolia-Okhotsk collisional belt, Trans-Baikal region (Russia) and Mongolia. *Tectonophysics* 306, 33–56. doi:10.1016/s0040-1951(99)00042-6